STRUCTURAL CHARACTERIZATION OF $In_2Ga_2ZnO_7$ CRYSTALLIZED BY MILLISECOND HEATING

A Thesis

Presented to the Faculty of the Graduate School

of Cornell University

In Partial Fulfillment of the Requirements for the Degree of

Master of Science

by

Katherine Kiera Jane Quinn

May 2019

ABSTRACT

The growing overall size and pixel density of large flat-panel displays will demand commensurate improvements to the semiconducting active materials used in thin film transistor (TFT) backplanes. Literature suggests that TFTs fabricated in crystallized compositions within the $(In_2O_3)_x(Ga_2O_3)_y(ZnO)_{1-x-y}$ ternary system (IGZO) will exhibit high mobility with controllable carrier concentrations, while also reducing trap states and electrical instabilities associated with amorphous IGZO TFTs. In this work, we examined the structural properties of IGZO alloys near the equimolar composition ($In_2Ga_2ZnO_7$) which were crystallized using laser spike annealing (LSA) at targeted peak temperatures ranging from 1000 to 1600 °C for dwell times from 250 μs to 10 ms. Films were sputter deposited from an IGZO target in 10% O_2/Ar ambient to produce 140 nm thick amorphous films which were subsequently annealed using the lateral gradient LSA method. The resulting crystallized structures were characterized using ~10 μm spatially resolved wide-angle X-ray scattering (11.3 keV) and optical reflectance (400-1000 nm). X-ray analysis shows no change in crystallization behavior for peak targeted temperatures from 1400-1600 °C, which we believe resulted from melting of the Si substrate and this limited actual temperatures to a 1414 °C maximum. Two similar crystalline structures were observed and tracked over annealing conditions. The first structure appears consistently over the entire range of anneal conditions. We propose a model for this crystal structure consisting of ordered planes of random cation composition. The onset temperature for this first crystallization was determined to be 1280 $\pm$ 50 °C. The second structure emerges in coexistence with the first one at dwells above 350 μs, indicating a

kinetically limited structural transition. We model the second structure as a superstructure of In_2O_3 planes separated by one or two layers of Ga and Zn cations in a random solution. The onset temperature for this second crystalline transition is 1395 $\pm$ 15 °C. Optical reflectance results do not correlate with X-ray crystallization transition regions and instead demonstrate densification behavior that increases with anneal temperature and relaxes with longer dwell times. Continued research and technique development to study the structural properties and crystallizing conditions of IGZO alloys are critical to identifying future candidate compositions for display TFTs.

BIOGRAPHICAL SKETCH

Katherine Quinn graduated with her B.S. in Materials Science and Engineering from Cornell University in 2018. During her time as an undergraduate, she became involved with Professor Michael Thompson's group in 2017 on the IGZO project. Her undergraduate work focused on the impact of millisecond annealing on the electrical properties of IGZO films. Katherine has also been involved in several extracurriculars in her time at Cornell, including taking on leadership roles in Engineers for a Sustainable World and Cornell Materials Society, and working as a Resident Advisor for four years. Katherine has decided to pursue a career in materials research and development and will be joining General Electric at their Global Research Center following graduation in 2019

.

ACKNOWLEDGMENTS

During my time at Cornell, I came to realize that luck and hard work can only get you so far and to be successful, you cannot be afraid to ask for help. This is the most important lesson I take from my undergraduate and graduate programs and I would not be where I am today without the support of individuals who were willing to offer help when I needed it.

I would first like to thank my parents and family for always supporting my aspirations and ambitions while keeping me grounded. I appreciate all the sacrifices you made to give me the opportunity to attend Cornell.

To my advisor, Professor Thompson, it has been a memorable time doing research in your group and I appreciate how much I have learned from working with you. I could not have overcome the experimental challenges I encountered without your help.

I would be remiss without thanking the Thompson group members who welcomed me in 2017, especially David Lynch for recruiting an aimless undergrad to carry on the IGZO project and learn how to make TFTs. Your endless patience answering my questions reassured me and turned me into a cool and confident cleanroom user.

To Emily Cheng, I am thankful for our late night rant sessions and your friendship over the past two years and I cannot wait to work with you at GE!

I would also like to thank the rest of the current Thompson/van Dover group members for your help and advice during this process and never failing to put a smile on my face. Good luck!

Thanks to the CCMR, CHESS, and CNF staff for helping with my experiments.

Finally, I would like to thank Gabe Joseph and Anna Lochte for being there through the good times and the bad. I am so grateful for your support and encouragement from afar. Thank you for always believing in me and I promise I will come visit soon.

TABLE OF CONTENTS

LIST OF TABLES

LIST OF FIGURES

CHAPTER 1

INTRODUCTION AND BACKGROUND

1.1 Introduction

As the flat panel display industry moves toward high efficiency, large area displays, there is a growing demand for semiconductor materials that can meet the needs of this evolving technology. The actual thin film semiconductor materials play a critical role as the active layer in thin film transistors, which act as switches to control the intensity of individual pixels.

1.2 Current Technology

Traditionally, amorphous semiconductor materials have been favored in TFTs due to their high area uniformity and lack of grain boundaries [1], with hydrogenated amorphous silicon (a-Si:H) serving as the primary industry workhorse for past 30 years [2].

However, drift mobility in a-Si:H occurs by hopping between localized tail states, which limits the field effective mobility of a-Si:H TFTs to < 2 cm^2/V-s. This property of a-Si:H, coupled with the instability of its TFTs under electric field stress, make this material difficult to use in OLED and high-resolution displays [3], [4]. While polycrystalline silicon (poly-Si) shows much higher electron mobility (~100 cm^2/V-s), and techniques have been developed to fabricate poly-Si on glass substrates [5], the presence of grain boundaries in polycrystalline Si limits its large area uniformity and causes off-state leakage current to be substantially higher than in a-Si [6].

1.3 Amorphous Oxides

Over the past two decades, various oxide semiconductors have been explored as alternatives to a-Si:H and poly-Si. In oxides, the strong iconic attraction between metal and oxygen atoms stabilizes an electronic structure in which the valence band is formed by occupied oxygen p-orbitals and conduction occurs in unoccupied metal s-orbitals, as shown in Figure 1.1 [1]. In crystalline oxides like ZnO and In_2O_3, the large, nearly spherical metal s-orbitals form a well-

dispersed conduction band which enables a small effective electron mass (0.25-0.35 m_e) and high electron mobilities (~200 cm^2/V-s). Unlike their Si counterparts, oxide semiconductors do not lose their favorable conduction properties and high electron mobilities with amorphization. While the highly directional sp^3 bonding orbitals in crystalline Si become strained in the amorphous structure and restrict carrier mobility, the metal s-orbital conduction pathway of crystalline oxide semiconductors is relatively unperturbed by amorphization, as seen in Figure 1.1 b. The large overlap between conduction orbitals is uncompromised in the amorphous state, fueling ongoing interest in amorphous oxide semiconductors (AOSs) for their high area uniformity (necessary for large displays) and their ability to maintain suitable carrier mobilities for glass-based substrates and future flexible electronics [7].

Nomura *et al*. outlined criteria of AOS material properties required for high-performance TFTs. The ideal material would have a stable and uniform amorphous phase that can form at relatively low processing temperatures, a high carrier mobility (>10 cm^2/V-s), and a controllable carrier concentration at low levels (~10^{15} cm^{-3}) [7]. It has been found that carrier mobility can be improved in AOSs by incorporating heavy post-transition metal elements with large s-orbitals to

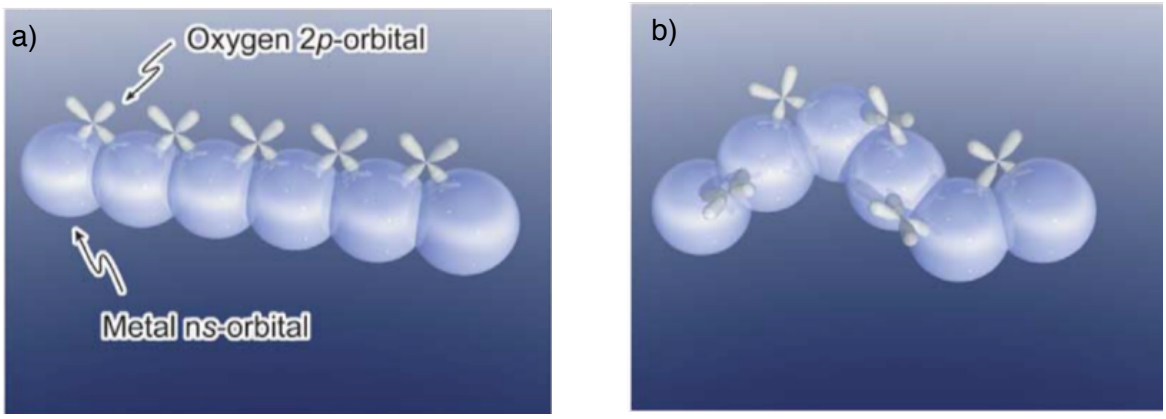

Figure 1.1 Conduction pathway along unoccupied s-orbitals in a) crystalline and b) amorphous transition metal oxides. Unlike in a-Si:H, the conduction pathway in crystalline transition metal oxides is unperturbed in amorphous form. Reference [3].

promote the formation of a well-dispersed conduction band. This motivates material systems that include In_2O_3 and ZnO. The controllability of carrier concentration is primarily influenced by the concentration of oxygen vacancies as they contribute free electrons. The concentration of oxygen vacancies can be restrained by incorporating strong metal-oxygen bonds. Ga-O is one such bond, thus motivating the inclusion of Ga in a potential AOS material system. As a result, material systems such as In_2O_3-Ga_2O_3-ZnO are seen as promising candidates to replace a-Si:H.

1.4 Amorphous IGZO

In particular, in 2004 Nomura *et al.* showed that amorphous oxide semiconductors from the In_2O_3-Ga_2O_3-ZnO (IGZO) material system exhibited promising electrical characteristics [3].

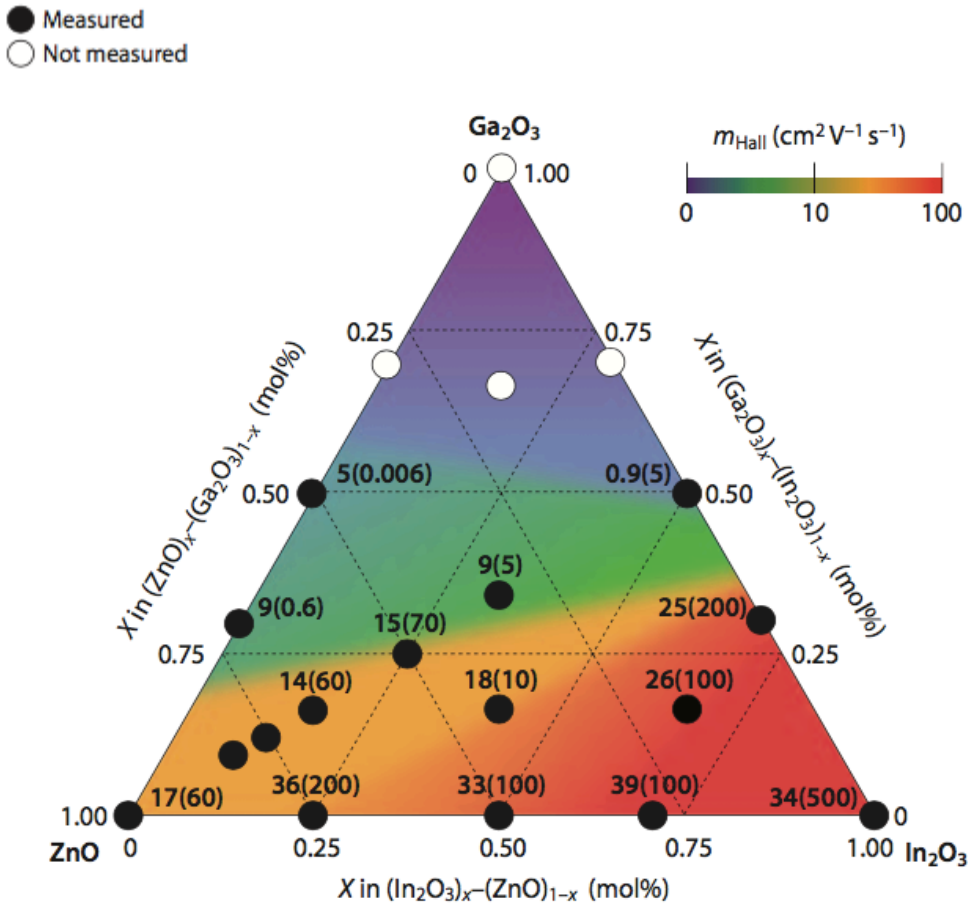

Figure 1.2 Ternary IGZO system. Hall mobility and carrier concentration (in parentheses, 10^{18} cm^{-3}) were measured for different compositions in the material system. Filled circles indicated compositions with measured values. Reference [3].

Nomura found that a broad range of amorphous IGZO compositions exhibit high carrier mobility (>10 cm^2/V-s) and a good control of carrier concentration (< 10^{15} to 10^{20} cm^{-3}), factors which are crucial for the fabrication of high-performance devices. Figure 1.2 shows carrier mobility and carrier concentration measured across the In_2O_3-Ga_2O_3-ZnO ternary system. Pure In_2O_3 and ZnO films crystallize during room temperature deposition and the carrier concentration is difficult to control. Similarly, the binary systems In_2O_3-ZnO (a-IZO) and In_2O_3-Ga_2O_3 (a-IGO) showed poor control of carrier concentration and devices in these compositions exhibited large leakage currents. Pure Ga_2O_3 films proved difficult to dope. But the ternary a-IGZO system proved viable and could be deposited with a controlled carrier concentration, which was achieved by oxygen partial pressure control during deposition. For example, devices fabricated with the nominal composition $InGaZnO_4$ exhibited stable carrier concentration and a reasonable Hall mobility of ~10 cm^2/V-s. Compositions along the pseudo-binary between $In_2Ga_2ZnO_7$ and ZnO similarly demonstrated reasonably high carrier mobility [7].

1.5 Electrical instabilities

However, the widespread adoption of amorphous IGZO in the display industry has been impeded by electrical instabilities that impair the performance of its TFTs. Devices fabricated with a-IGZO experience drifts in turn-on voltage over time, resulting in shifts in pixel brightness and reduced device lifetime. These instabilities originate from sub-gap defect trap states in the amorphous structure and are aggravated by stress factors experienced during TFT operation. Most stress factors can be described as bias temperature illumination stresses and promote carrier trapping and defect state relaxation in TFTs used at elevated temperatures or under illumination [2].

While the particular mechanism of device reliability deterioration is debated, when it comes to resolving the electrical instabilities seen in a-IGZO, many researchers have focused

on the origin of the instabilities by reducing the material's sub-gap defect states [8], [9]. Some researchers have attempted to address these challenges by using different sample geometry, passivation layers, and annealing regimens to modest success [9]–[13]. Others have concentrated on altering the amorphous structure to reduce defects [14], [15]. Similar to a-Si:H, most sub-gap defect states in IGZO are related to the disorder of the amorphous structure and thus can be reduced through crystallization [15].

1.6 Crystal structure of IGZO

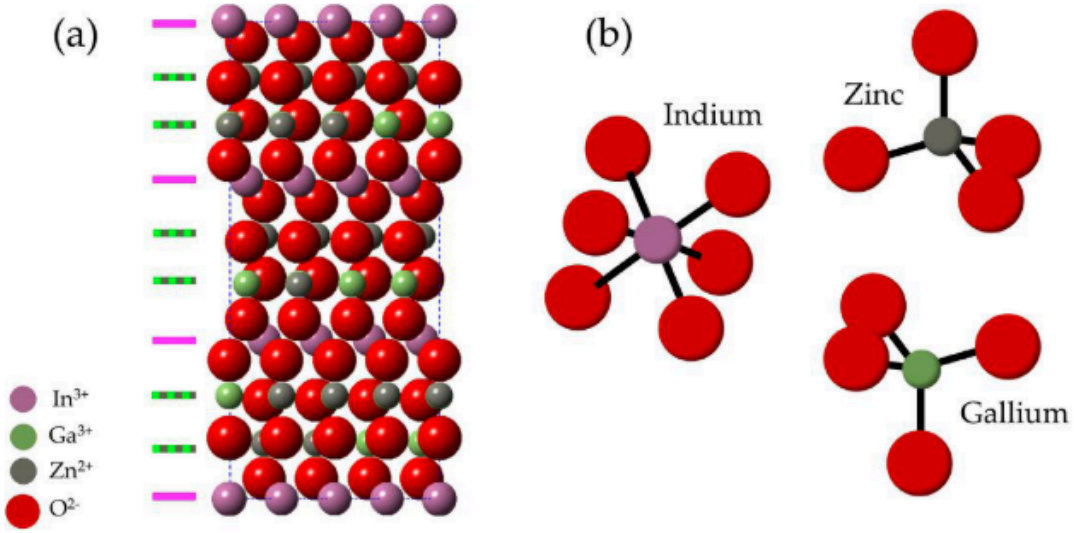

Figure 1.3 (a) $InGaO_3(ZnO)$ depicted as a space-filling model along the (001) axis. In cation planes are pointed out by the magenta lines while mixed Ga/Zn cation planes marked by the mixed green and gray lines to the left of the model. (b) Models of cation coordination. In is octahedrally coordinated within the anion sublattice while Ga and Zn adopted a distorted tetrahedral arrangement. Reference [2].

Kimizuka *et al.* was the first to study the structure of IGZO compounds in 1985 by synthesizing single crystal $InGaO_3(ZnO)_m$ powder compounds from constituent In_2O_3, Ga_2O_3, and ZnO powders [16]–[18]. IGZO compounds fall under what are called homologous oxides with the formula $RMO_3(ZnO)_m$ (R = Sc, In; M = Al, Ga, Fe) with a structure composed of m ± (M/Zn)-O blocks sandwiched between alternating RO_2 layers [19]. Kimizuka found that $InGaO_3(ZnO)_m$ is isostructural with $InFeO_3(ZnO)_m$ and both compounds adopt $R\bar{3}m$ symmetry when m is odd and

$P6_3/mmc$ when m is even. An example structure for $InGaO_3(ZnO)_m$ for m = 1 composition is shown in Figure 1.3.

In 2004, Nomura *et al*. formed single crystal $InGaO_3(ZnO)_5$ films through reactive solid-phase epitaxy from a 2 nm-thick ZnO epitaxial layer on a yttria-stabilized-zirconia substrate [20]. Single crystal IGZO seeds formed from a solid-phase reaction between the ZnO epitaxial layer and pulse-laser-deposited (PLD) polycrystalline IGZO and grew much faster in the lateral direction than in the c-axis direction across InO_2 layers. Chen *et al*. grew single crystal IGZO films through a similar reactive solid-phase epitaxial technique but sputter deposited IGZO for a more cost-effective fabrication [21]. Chen also grew single crystal films on ZnO epilayers by annealing in a ceramic ZnO box to prevent composition variation. Nomura's electrical characterization of single crystal IGZO films shows a manageable carrier concentration of less than 2×10^{18} cm^{-3} and Hall mobility above 10 $cm^2/V\text{-}s$. When these films were fabricated into TFTs, the devices exhibited mobilities of 80 $cm^2/V\text{-}s$ [22], [23]. Despite these promising electrical characteristics, the complicated epitaxial growth and high-temperature annealing techniques required to produce single crystal IGZO proved impractical for large-scale implementation in flat panel display applications.

1.7 Annealing Methods

Annealing has traditionally been used in IGZO TFT processing to address instability problems found in devices fabricated with as-deposited amorphous structures [37]. Postdeposition annealing of amorphous films was reported to alter the amorphous structure, improve oxygen compensation, and reduce the tail state defects that are the origin of said device instabilities [38], [39]. In 2003, Nomura *et al*. first demonstrated TFTs fabricated from single crystalline IGZO by high temperature postdeposition furnace annealing at 1400°C [23]. Such temperatures are impractical for industrial processing and limit device fabrication on glass or flexible substrates.

Although more realistic processing regimes were offered when c-axis aligned IGZO was demonstrated as a result of deposition on a substrate heated to 300°C, other phases are inaccessible through this technique and annealing during deposition makes it difficult to study crystallization and growth kinetics [40]. Millisecond timescale lateral gradient laser spike annealing is favored as a fast, high-throughput technique for studying a material's structural evolution as a function of annealing. Bell *et al*. demonstrated this novel technique could be used to access a range of material properties across spatially resolved thermal gradients on a single sample [41]. Chung *et al*. first used this technique with IGZO to laser spike anneal amorphous films at 300-500°C [42]. This work found a marked increase in TFT mobility (~70 cm^2/V-s) as a result of laser spike annealing the films, however the degradation of TFT properties over time suggests the structural relaxation of metastable phases.

Laser spike annealing is a non-destructive technique that has the advantages of short annealing timescales and localized annealing. Not only can LSA enable access to metastable film morphologies, but it has recently been utilized to study the crystallization and growth kinetics over a range of IGZO compositions [2], [36]. The potential of laser spike annealing to access metastable phases of IGZO motivates the use of this technique in furthering structural studies of this material system.

1.8 Polycrystalline IGZO

IGZO is most commonly found as a polycrystalline structure composed of small, untextured single crystal grains. Amorphous IGZO only crystallizes upon annealing to 600-800°C and, while novel solution-processing techniques have reduced the required annealing temperature for crystallization, devices fabricated from polycrystalline IGZO show degraded performance with low mobilities (~1-3 cm^2/V-s) due to grain boundary carrier trapping [7], [15], [24], [25]. Work by Zhu *et al*. showed access to a range of structural space from amorphous to polycrystalline IGZO

by varying deposition parameters like target composition, O_2 fraction in the sputter gas, RF power, and temperature during sputter deposition [26]–[28].

1.9 CAAC-IGZO

A recent area of focus has been on a crystal structure lying between polycrystalline and amorphous IGZO called c-axis aligned crystalline IGZO. In 2012, Yamazaki *et al*. reported success in fabricating a crystalline form of IGZO showing c-axis alignment like a single crystal but with a mosaic pattern in the a-b plane and an absence of clear grain boundaries [29]. This structure stands in contrast to a polycrystal that shows random a-, b-, and c-axis alignment and clear grain boundaries. This highly textured alignment makes the CAAC-IGZO structure closer to a single crystal than an amorphous structure. Cross-sectional imaging shows the film has a layered structure similar to the diagram in Figure 1.3.

TFT devices fabricated with CAAC IGZO show promising electrical characteristics. Devices exhibited extremely low off-state current (~100 yA/μm) and high reliability when tested under positive and negative bias stress [4]. This improved reliability seen in CAAC IGZO is attributed to a reduction in sub-gap defect trap states by 2-3 orders of magnitude compared with a-IGZO [30]. TFTs fabricated with CAAC-IGZO also exhibit an avalanche breakdown voltage almost six times greater than that of single-crystal Si [31]. While CAAC IGZO FETs show a mobility on par with a-IGZO FETs (7.7 cm^2/V-s), films of this structure show no grain boundary trapping effects and display large area uniformity [32]. With the fabrication of CAAC IGZO also came news that CAAC IGZO transistors were successfully implemented in OLED 4k and flexible display applications and a memory cell. As of 2012, Sharp Corporation had developed smartphones, tablets, and 4k Ultra HD displays based on CAAC-IGZO technology [33].

With such favorable and practical electrical and structural properties, a great deal of research has been concentrated on understanding the factors controlling growth and

crystallization of CAAC IGZO. Yamazaki's theory of the formation of CAAC IGZO in sputter deposition suggest that small single crystal pellets sputter off the target and deposit on the substrate such that the c-axes are aligned [32]. However, more recent work by Chung and Lynch suggest a more classical nucleation and growth model regulated by sputter deposition parameters [2], [34], [35]. Prior to crystal nucleation, the first few layers of IGZO deposited are disordered. At elevated substrate temperatures, stresses in the disordered layer may provide enough driving force to spur crystal nucleation. At high enough temperatures, the crystal nuclei may coalesce and permit ordered crystal growth into the aligned CAAC structure.

Extensive work has been dedicated to determining the effect of many deposition parameters on CAAC formation. In 2015, Zhu *et al*. investigated the influence of substrate temperature and O_2 fraction in the reactive gas sputtering environment on CAAC alignment and crystallinity [27]. This study found that substrate temperatures ~315°C in a 10% O_2 deposition environment yield optimally aligned CAAC IGZO. The researchers also observed that the etch rate of highly aligned CAAC IGZO in 5% HCl by volume is 10 times slower than the etch rate for amorphous IGZO, suggesting that etch rate is highly correlated to crystallinity [26]. These studies suggested a nucleation based growth model in which elevated substrate temperatures increased surface mobility enough to enable nucleation and development of a ordered growth [28]. They also demonstrated the effect of deposition parameters like O_2 fraction and substrate temperature on Zn-content in the film, observing increasing Zn-content in films sputtered at low pO_2. This trend corresponds with regions of increased texturing, suggesting CAAC formation is enhanced in parameter spaces favoring Zn-rich films.

1.10 Crystallization kinetics of the IGZO series

The results of these works clearly demonstrate the bearing of film composition on crystallinity. This was further investigated in 2016 when Roach studied superlattice formation by post-

deposition laser spike annealing (LSA) across seven different $InGaO_3(ZnO)_m$ compositions as a function of Zn content [36]. This work identified five different equilibrium structures of $InGaO_3(ZnO)_m$ (each phase corresponding to a different m-value) and observed three unique phases produced through postdeposition annealing. This study's use of LSA enabled access to a range of peak annealing temperatures and dwell times. This resulted in the finding that onset crystallization temperature changed as a function of dwell time, indicating that the crystallization process may be a kinetically limited one.

In 2017, Lynch built on the models of superlattice formation originally theorized in Roach's work by exploring phase formation within the $InGaZnO_4$-ZnO pseudobinary using LSA [2]. Lynch found that $InGaO_3(ZnO)_m$ with compositions near m=1 crystallized into non-oriented polycrystalline structures with m > 1 stoichiometry. He suggested that this observed off-stoichiometry could be attributed to cationic disorder and posited that an ultimate In_2O_3 layered superstructure is formed at sufficient annealing time and temperature through intergranular diffusion.

1.11 Optical Methods

The optical properties of a material, such as its index of refraction n and extinction coefficient k, are strongly related to its structure. Traditionally, this principle has been applied as a rapid and sensitive technique to recognize phase changes. For instance, Valkenberg detected high-pressure phase changes in silver and cuprous halides by observing changes in birefringence. Bassett et al. furthered work along this vein by studying high pressure phase changes between iron polymorphs through changes in their optical reflectivity. More recently, a set of materials exhibiting large changes in optical properties have been classified as optical phase change materials and have been developed in tunable photonic applications. Changes in optical properties such as reflectivity are proven to be sensitive indicators of structural change. Thus,

studying the optical properties of IGZO as a function of annealing conditions may be used to identify structural transitions.

CHAPTER 2

EXPERIMENTAL

2.1 Sputter Deposition

Sputtering is a tunable and cost-effective thin film deposition technique that is frequently used for IGZO deposition due to its advantages. Sputtering is relatively simple and films can be deposited at room temperature. In addition, sputter deposition allows for fine stoichiometric compositional tunability through the control of gases to yield uniform, conformal compound films.

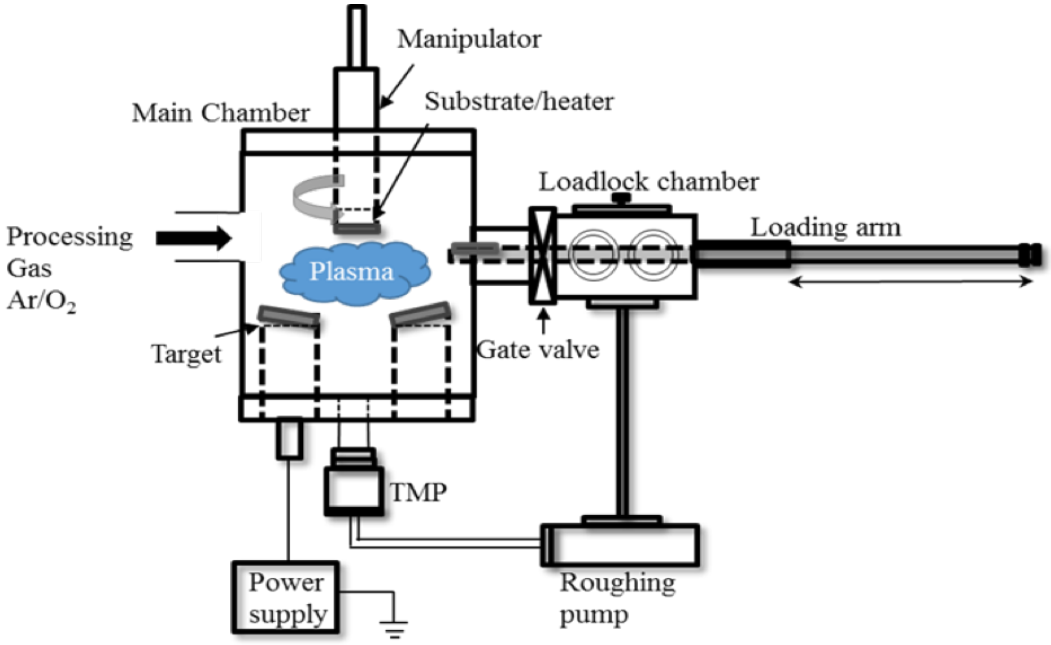

Figure 2.1 A diagram of the AJA RF Magnetron Sputter system used to deposit $In_2Ga_2ZnO_7$. A sintered polycrystalline $In_2Ga_2ZnO_7$ target was reactively sputtered with a 10 sccm gas mixture of 10% O_2 in Ar at 200 W RF power. Reference [1].

In this work, single crystal, heavily p-doped (100) Si (0.01-0.02 Ω-cm) wafers thermally oxidized with a 20 nm thick oxide layer. A single composition $In_2Ga_2ZnO_7$ (IGZO) thin film was deposited using a load-locked AJA reactive RF magnetron sputtering system as shown in Figure 2.1. The sputter system had a vacuum chamber with a base pressure of 10^{-8} Torr and the film was

deposited at room temperature. An oxide sputter target with a composition near 1:1:1 (In_2O_3:Ga_2O_3:ZnO) from the Kurt J. Lesker Company (99.99% purity) was used as source material. The target was presputtered for five minutes before opening the shutter to remove surface contaminants. A sputter pressure of 5 mTorr was used with a 10% O_2 in Ar gas environment and a total flow rate of 10 sccm. RF power was held at 200 W for the 30 min deposition to yield an approximately 138 nm thick film. The substrate was rotated at 20 RPM to achieve a uniform thickness.

2.2 IGZO Deposition Rate Calibration

The RF power supplied to the target is linearly related to the resulting deposited film thickness. Deposition rate calibrations for the $In_2Ga_2ZnO_7$ (IGZO) target were characterized in 2017 and again in 2019 (see Figure 2.2).

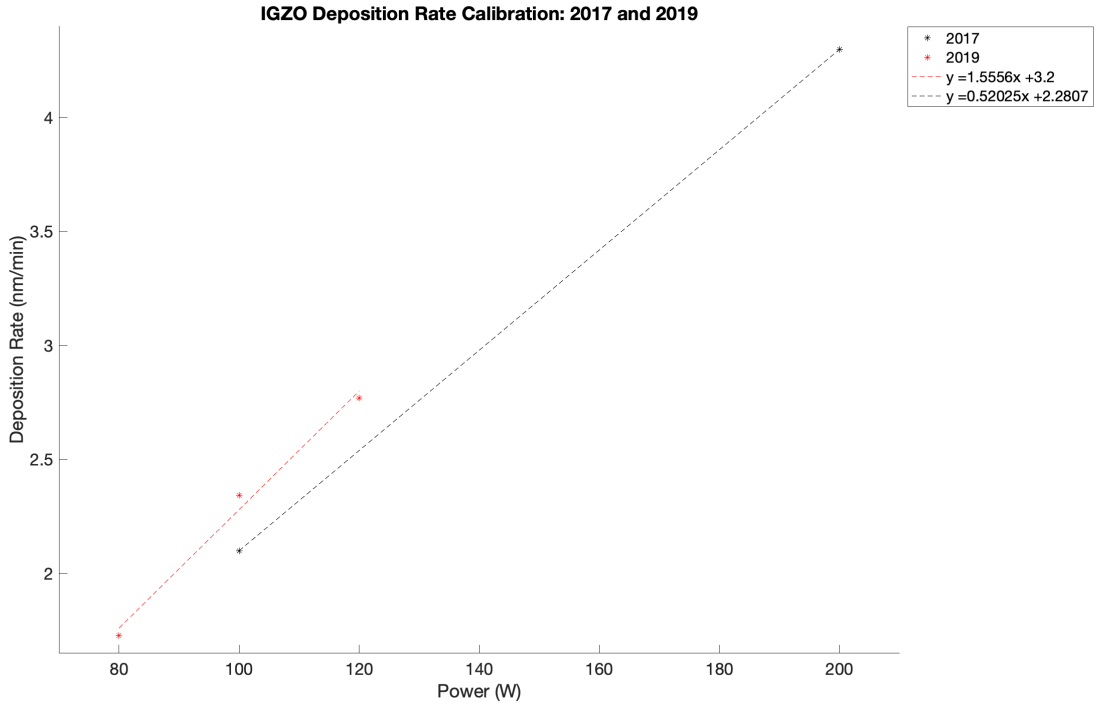

Figure 2.2 Film deposition rate vs. sputter power as characterized in 2017 and again in 2019. The deposition rates between 2017 and 2019 are relatively similar.

2.3 Film Thickness Measurement

In this study, a combination of profilometry and optical reflectance techniques were used to estimate the film thickness of deposited IGZO films. To measure film thicknesses by profilometry, IGZO films were photolithographically patterned using Microposit S1813 photoresist to achieve 5 mm x 50 mm structures. IGZO films were etched for three minutes in a dilute 5% HCl solution and photoresist was removed using acetone and isopropyl alcohol. Film thickness was determined by measuring the depth of the etched trench structures using contact profilometry on a P10 Profilometer.

Optical reflectance techniques were also used to estimate the thickness of a film based on the index of refraction and extinction coefficients over a range of wavelengths. Jianing Sun, Woollam applications engineer, assisted in developing a material model for IGZO to be used on a Woollam Spectroscopic Ellipsometer. Indices of refraction and extinction coefficients generated by this model were then used with a F20 Filmetrics for faster thickness measurements.

2.4 Laser Spike Annealing

Laser spike annealing uses a line-focused continuous wave laser beam that is scanned across a sample for controlled time durations. This annealing time is characterized by the dwell, which is defined as the laser FWHM divided by the scan velocity. In the lateral gradient laser spike annealing (lgLSA) technique, the beam is intentionally non-uniform orthogonal to the scanning direction to produce a lateral temperature profile (Figure 2.3). Using a Gaussian-like laser profile, the highest peak temperatures are achieved at the beam center with temperatures falling on either side as shown in Figure 2.3. This technique was used to irradiate the IGZO film with a CO_2 laser (10.6 μm wavelength, FWHM = 650 μm) with 625 laser stripes arranged in the randomly generated pattern shown in Figure 2.4. Stripes were irradiated with 30-60 W of laser

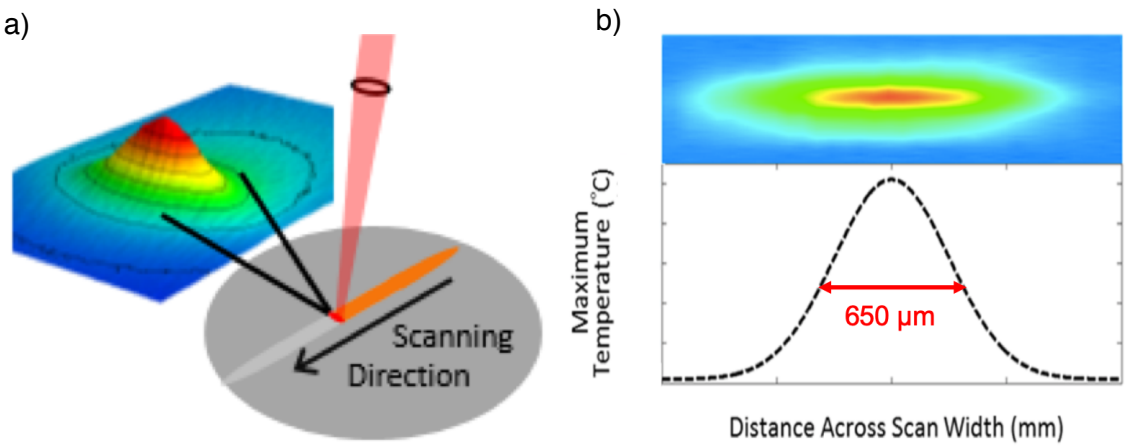

Figure 2.3 A schematic of a) laser spike annealing a stripe on a sample and b) the consequent lateral temperature gradient that is produced normal to the scan direction. The temperature gradient follows the laser profile and can be modeled as a Gaussian with a FWHM = 650 μm. In lgLSA, the peak targeted annealing temperature occurs at the center of the anneal stripe. Reference [39].

power at dwell times of 250 μs-10 ms to target peak temperatures between 1000 and 1600 °C. Temperatures are estimated based on bare Si wafers.

2.5 μ-WAXS from CHESS

Microbeam Wide Angle X-ray Scattering (μ-WAXS) was performed at the Cornell High Energy Synchrotron Source. As a diffraction techniques, μ-WAXS is used for structural characterization and of the short range order in a material. In this experiment, a 11.3 keV X-ray beam was focused to a 15 μm lateral spot size on the sample using capillary X-ray optics. Scattered X-rays reflected off the sample and were measured by an Eiger 1M area detector to produce a 2D map of x-ray intensities across the scan area.

Each LSA stripe was probed laterally across a 2 mm distance with a 10 μm step size to capture the effect of the lateral temperature gradient.

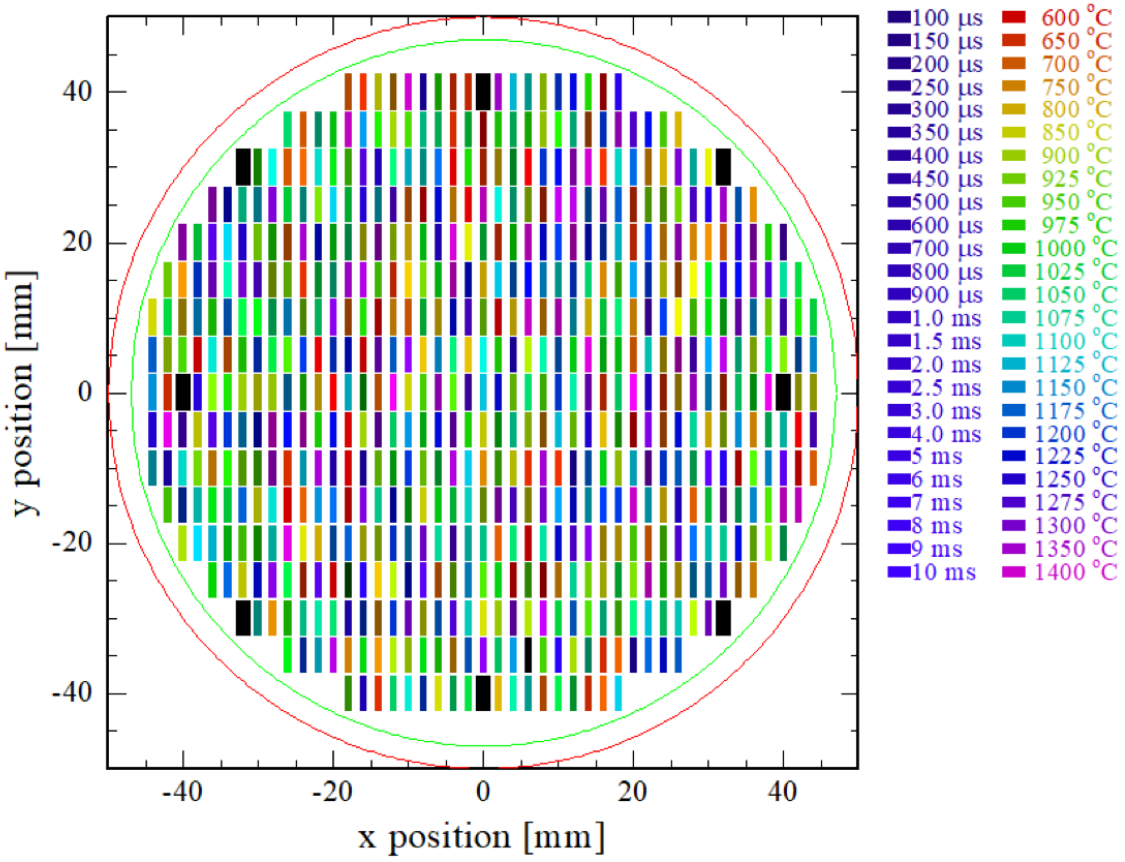

Figure 2.4 An example diagram of 625 LSA stripes of different target peak anneal temperatures and dwells randomly arranged on a sample. For this study, target peak anneal temperatures range from 1000 – 1600 °C and dwells from 250 µs – 10 ms.

Stripes were scanned in the order of decreasing relative peak anneal temperature then decreasing anneal dwell. Only stripes with relative peak annealing temperatures between 1500 and 1600 °C were successfully scanned during the allotted beam time at CHESS. Raw 2D data collected by the detector were azimuthally integrated to 1D data and then smoothed and normalized. The Bragg scattering angle θ can be related to reciprocal q-space through by

$$q = 4\pi\sin(\theta)/\lambda \qquad (2.2)$$

where λ is the X-ray wavelength. Reciprocal space q is related to the X-ray's change in momentum upon scattering with units of $Å^{-1}$. Integrated data takes the form of 1000 x 200

matrices accounting for 1000 X-ray intensity measurements across all of q-space for each of the 200 scans collected across the scan area. These data can be used to visualize the anneal behavior in a 2D plot of X-ray intensity vs. q-space for individual or multiple scans. Alternatively, data can be visualized in a 3D plot of q-space vs. intensity for all 200 scans.

2.6 Optical Reflectance Characterization

2.6.1 Theory

The optical properties of a material are most simply characterized by its index of refraction, n, and extinction coefficient, k. Different phases of a material will exhibit different n and k values. Thus, structural transitions in a material can potentially be identified using this rapid, non-destructive optical reflectance technique. Such a technique was developed and implemented in this work.

2.6.2 Determination of IGZO Optical Constants

Ellipsometry is another common optical technique which can be used to determine the n and k optical constants of a material by measuring the change in polarization as light reflects from a material. These constants can also be used to determine film thickness and are commonly used in thin film measurement systems. In basic ellipsometry measurements, polarized light of a single wavelength is directed at the sample surface and the reflected light is collected by a detector. The amplitude, phase, and polarization changes of the reflected light are measured to determine what fractions of light were reflected and absorbed by the sample. This information can be used to determine the index of refraction and extinction coefficient for that particular incident wavelength of light. Ellipsometry measurements often incorporate a range of incident light wavelengths to calculate the material's n and k values as functions of wavelength. Ellipsometry was performed on IGZO samples sputter deposited at 80, 100, and 120 W RF power with otherwise identical deposition parameters to those described above. Resulting n and

k values at a wavelength of 400.2 nm are shown in Table 2.1. As expected, these optical material constants are consistent within the sample set and are relatively insensitive to deposition rate and film thickness. A model of these optical constants, and corresponding range of measurement wavelengths, was loaded into a Filmetrics film measurement system to allow for rapid film thickness evaluation.

Table 2.1 List of refractive indices at λ = 400.2 nm for $In_2Ga_2ZnO_7$ films deposited at 80, 100, and 120 W. The refractive indices are used to create Filmetrics material models for film thickness measurements.

Sputter Deposition Power (W)	Refractive Index n at λ=400.2 nm
80	2.0967 ± 0.0254
100	2.1049 ± 0.0104
120	2.1583 ± 0.014

2.6.3 Optical Relfectance Experimental Set Up

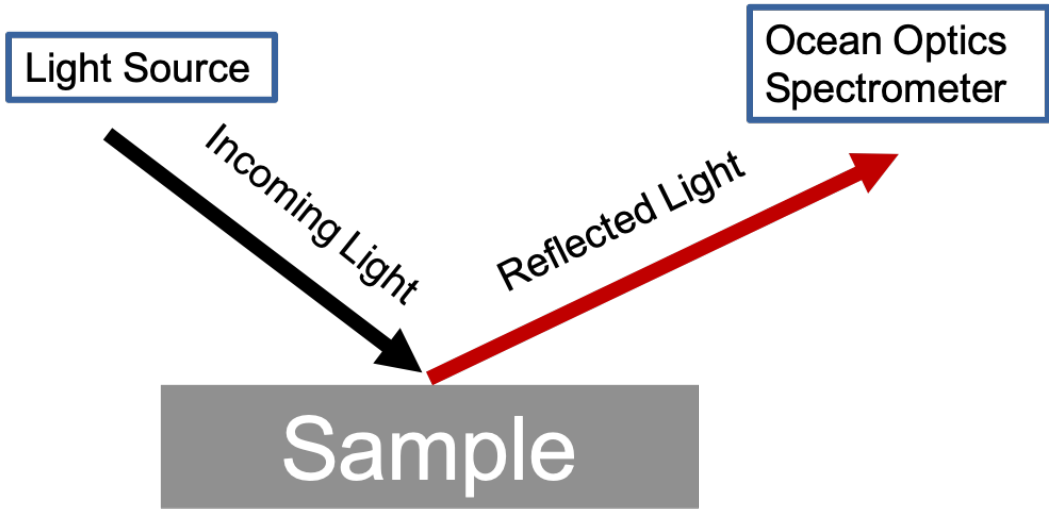

Figure 2.5 A schematic of the optical reflectance setup. White light is shown at a the sample close to anneal stripes and reflected light of wavelengths 400-1000 nm is measured by a spectrometer.

An optical reflectance setup was designed for rapid, automated capture of the reflection signal of a small area of a material annealed by LSA. This experiment was designed to collect optical reflectance information across the lateral profile of an LSA stripe to potentially identify regions of structural transition. A diagram of the experimental setup is shown in Figure 2.5. The sample sits on an x-y motion stage and is illuminated by a white light source. The white light passes through an Ocean Optics Spectrometer to measure the reflected wavelength and intensity. Reflected light is collected from a small area by fiber. This reflected beam is then measured by a spectrometer. The setup also includes a camera for image capture.

2.6.4 Data Collection

Blank and mirror reflectance signals are collected by measuring light reflected off an opaque, non-reflecting surface to account for background signal and measuring light reflected off a perpendicular mirror to account for complete reflectance. These measurements are collected throughout the experiment. Then a 10 μm diameter light beam is focused at 25 points around the sample to account for film thickness variation, wafer and stage tilt, and nonuniformity. Data collection is performed as specified by a job file listing the wafer coordinates and anneal conditions of each laser stripe. The stage navigates to align each laser stripe and reflectance signals are collected for wavelengths of 340-1026 nm over a 101 μm x 10 μm area vertically and horizontally centered about the stripe center.

2.6.5 Data Processing Procedure

Averaged blank and mirror reflectance signals were used to normalize raw reflectance data collected at each stripe according to the formula

$$\frac{\text{Raw Data} - \text{Blank Data}}{\text{Mirror Data} - \text{Blank Data}} \tag{2.3}$$

In addition, data was scrubbed and smoothed using a Savitzky-Golay smoothing filter in Matlab, which was a moving average with filter coefficients determined by an unweighted linear least-squares regression and a two-degree polynomial model.

CHAPTER 3

X-RAY STRUCTURAL CHARACTERIZATION

3.1 Introduction and Overview

This section describes the analysis and interpretation of structural data collected using μ-WAXS at CHESS. Data measured by the Eiger 1 M area detector were radially integrated using pyFAI to convert 2D area data to 1D Intensity vs. 2θ line scans. This 1D data is represented by 1000 x

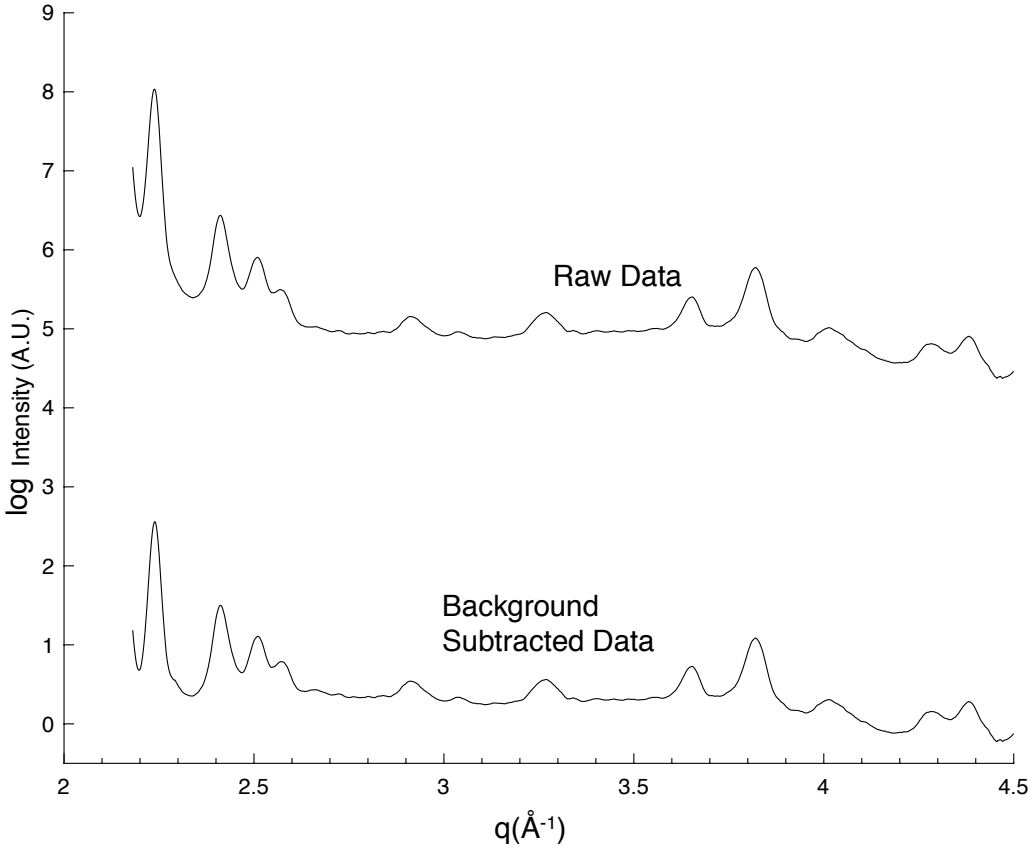

Figure 3.1 Example Intensity vs. q-space plot of raw and background subtracted data for $In_2Zn_2GaO_7$.

200 matrices accounting for 1000 X-ray intensity measurements across all of q-space for each of the 200 scans collected across the 2 mm scan area centered about each LSA stripe. This raw data was scrubbed of anomalous points, normalized, and smoothed with a low-pass Savitzky-Golay filter in Matlab, which was a moving average with filter coefficients determined by an

unweighted linear least-squares regression and a two-degree polynomial mode. X-ray scattering due to air was subtracted from the data to show only scattering from to the IGZO film. The background was modeled as linear within four primary peak regions. An example of the raw data and background subtracted data are shown in Figure 3.1.

Due to CHESS beamtime constraints, X-ray measurements were only obtained for 115 of the 625 LSA conditions. These included stripes annealed at the highest peak temperatures (1500, 1525, 1550, 1575, and 1600 °C) where crystallization would be more likely, over a broad range of dwell conditions. 200 X-ray scans were collected across the stripe; hence this data subset contains 23,000 individual diffraction scans and is rich with potential structural information. Given the size of the data, it is impractical to approach diffraction analysis scan by

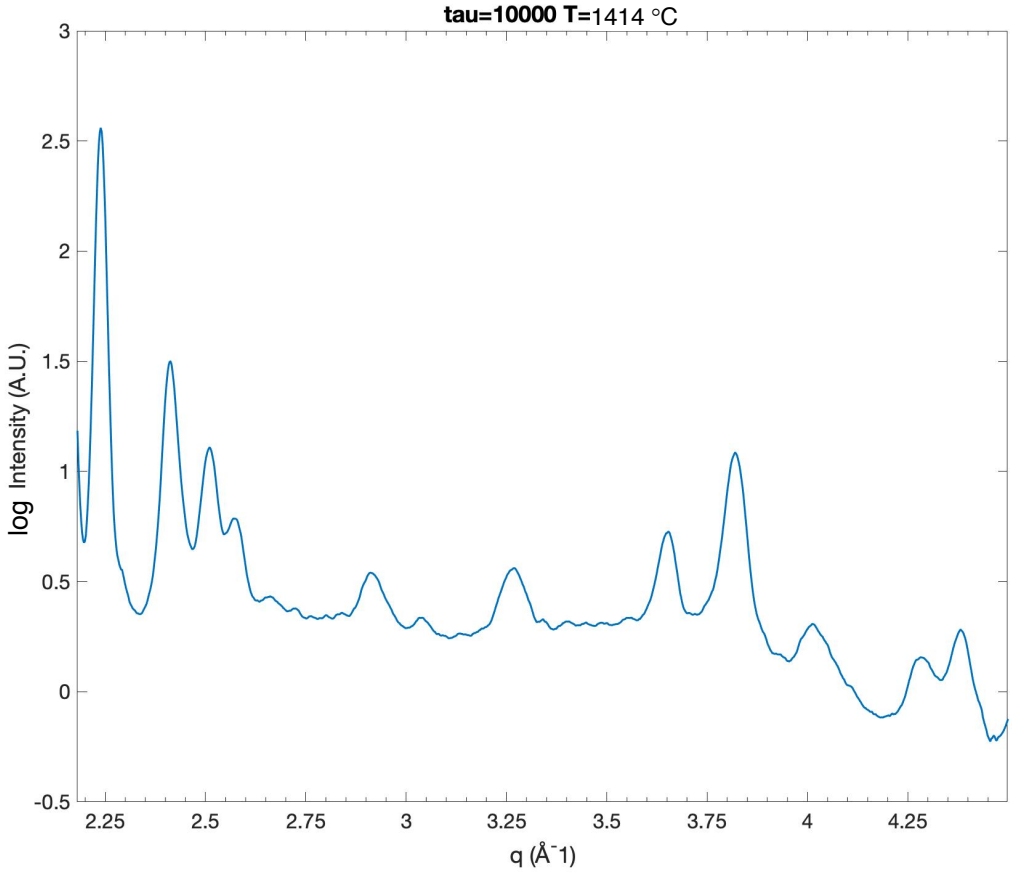

Figure 3.2 Example Intensity vs. q-space for a stripe annealed at targeted peak temperature of 1600°C and dwell of 10 ms.

individual scan. In the effort to look for broader structural trends as a function of annealing temperature and dwell, it was necessary to visualize the Intensity vs. 2θ line scans collectively in a more compact form.

Figure 3.2 shows an example Intensity vs. q-space plot for a stripe annealed at 1600°C with a 10 ms dwell taken from the center of the anneal stripe. The appearance of sharp, distinct peaks is evidence of crystallization. To rapidly compare significant peaks and compare peak prominence, 3D data visualization was critical.

This was accomplished by representing the 1D data with colormaps. Figure 3.3 shows an image group where q-space is plotted on the y-axis, distance on the x-axis, and intensity reflected as a color from dark blue (low intensity) to bright yellow (high intensity). Each vertical line is one of the 200 individual X-ray diffraction patterns measured across the scan area. Each horizontal "bar" represents the appearance of the peaks existing on individual line scans (Figure 3.2). Visualizing X-ray diffraction data in this way enables more rapid screening for

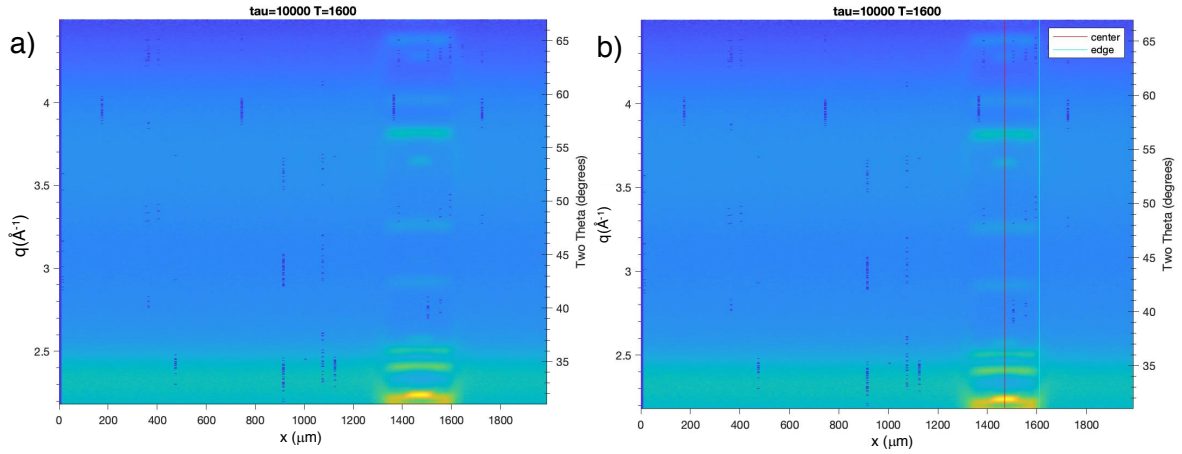

Figure 3.3 a) Example colormap for 200 scans across a stripe annealed at targeted peak temperature of 1600°C and dwell of 10 ms and b) overlaid with a center and edge determined by the center- and edge-finding algorithm.

crystallization and identification of regions of interest. This method of representation also makes

clear a distinct edge between the unannealed, amorphous regions (outer regions of the stripe) and the annealed region containing peaks from crystallization. As the lgLSA technique produces a decreasing annealing temperature profile moving outward from the stripe center, this amorphous to crystalline edge is expected to correspond to a particular annealing temperature, the critical onset temperature for the amorphous to crystalline structural transition.

3.2 Center and Edge Finding Algorithm

Determining this transition temperature requires first the determination of the stripe center and the transition edges. Both positions were determined using an algorithm which scans along the stripe region of interest and, at each point, compares the intensity signals to the immediate left and right of each scan. Assuming the lateral gradient temperature profile is symmetric about the LSA stripe center (represented by Figure 2.3), these scans to the immediate left and right should be most similar when the scan position is at the stripe center. Thus, the algorithm determines the stripe center to be the position where there is minimum difference to the left and right. Conversely, the intensity signals at a transition edge should change abruptly. Figure 3.3b shows the results of this center- and edge-finding algorithm plotted on the same stripe shown in Figure 3.3a. In this example, the center is found to occur at 1480 μm and the edge at 1610 μm. The alignment of the calculated center and edge confirms the algorithm to determine these positions.

3.3 Identification of onset crystallization temperature

The onset crystallization temperature is determined from the position of the stripe edge through the lateral temperature gradient produced by LSA, which can be approximately modeled as a Gaussian function of the form

$$T = T_{peak} e^{\left[-\frac{\left(\frac{h}{\sigma}\right)^2}{2}\right]} \quad (3.1)$$

Where T_{peak} is the peak temperature at the anneal stripe center, h is distance from the center to the transition edge, and σ is the standard deviation of the temperature profile. This standard deviation can be related to the full width half maximum as

$$FWHM = 2\sqrt{2 \ln 2}\,\sigma \quad (3.2)$$

Although the FWHM of the temperature profile is the appropriate value, in this work we

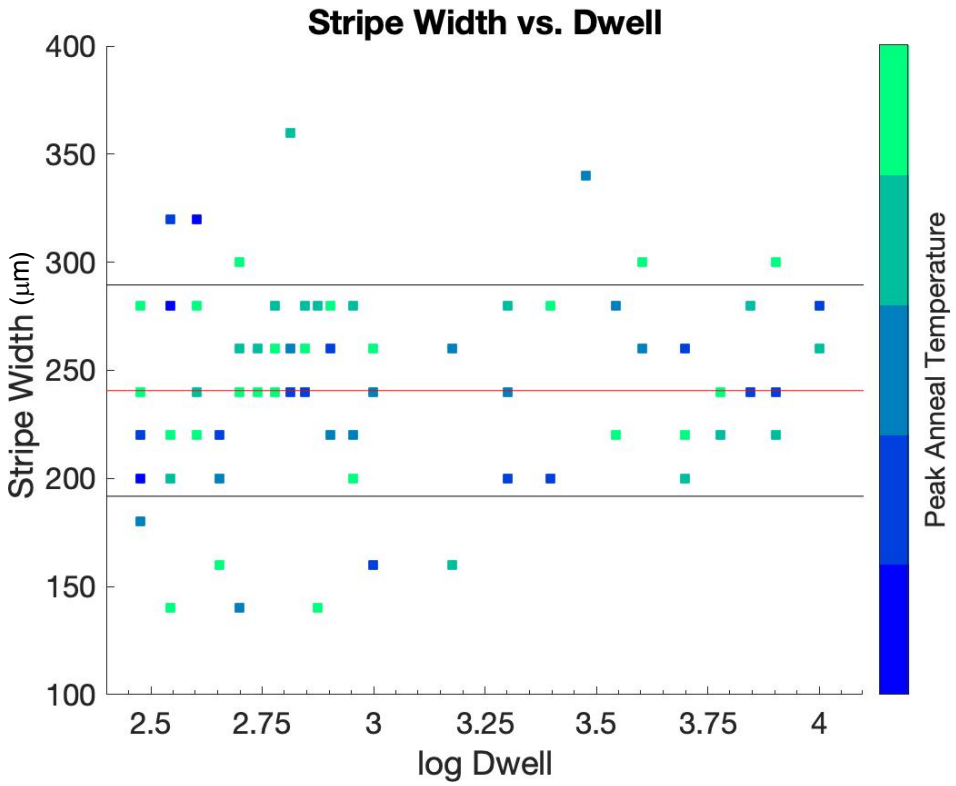

Figure 3.4 Estimated width of the crystallized region by dwell and color-coded by target peak temperature 1500-1600 °C. The mean (red) and a standard deviation above and below the mean (black) are shown.

approximate it as equal to the FWHM of the annealing laser, 650 μm. The FWHM, stripe halfwidth, and an estimated peak temperature of each stripe are then used to determine the temperature at the transition edge. Figure 3.4 first shows the estimated stripe width across all

dwells and targeted peak temperatures between 1500-1600 °C. There is no clear trend in stripe width with increasing dwell or peak temperature. This conflicts with the expectation that stripe width should increase with peak temperature as predicted by Equation 3.1. It is likely that the transition temperature decreases weakly with increasing dwell also, but this should be a weaker effect. These trends were demonstrated in previous anneal studies of IGZO and were used to infer a kinetically limited crystallization [34].

The absence of any T_{peak} dependence in Figure 3.4 suggests that all of the measured stripes were annealed at the same peak temperature. This may be explained by considering the targeted annealing temperatures relative to the melting points of the annealed materials. While the melting points of compositions in the $InGaO_3(ZnO)_m$ series have not been well characterized, the m = 0.45 composition film used in this study did not show any evidence of melting during the anneal process, thus it is fair to assume the film remained in the solid state over this range of annealing conditions. The film was deposited on a heavily-doped, single crystal Si substrate, however, and the melting point of Si is well-established as 1414 °C at standard conditions. Given that the targeted anneal conditions spanned peak temperatures of 1000-1600 °C, the peak temperature anneals may have surpassed the Si melting point resulting in melting of the substrate. In the liquid state, Si becomes a metallic and reflects nearly all IR radiation, reducing the laser power coupled into the substrate [43]. This means that beyond 1414 °C, subsequent increases in laser power would not result in increased peak temperatures on the film. In this model, all stripes ostensibly annealed at temperatures above 1414 °C, including the X-ray characterized stripes annealed over 1500-1600 °C, were effectively annealed at one peak temperature, 1414 °C.

The model of a single peak anneal temperature of 1414 °C due to substrate melt and laser decoupling is the most probable explanation behind the absence of trends between stripe

width and T_{peak}. Thus, for all subsequent analysis it will be assumed that all stripes targeted for annealing at temperatures above 1414 °C were actually just annealed at T_{peak} = 1414 °C.

3.4 Structural Analysis Overview

The initial transformation is characterized by bands (particularly strong peaks at q ≈ 2.2, 2.5, and 3.8 $Å^{-1}$ in Figure 3.3a) that extend across the entire width of the crystallized region. The second transformation is marked by other bands (weaker peaks at q ≈ 2.5 and 3.7 $Å^{-1}$) that are narrower (~50 μm compared to ~200 μm wide crystalline region). X-rays may indicate two distinct structural transformations; amorphous IGZO to crystal and a second transformation at higher temperature (closer to the center of the laser stripe). As the bands corresponding to the first transformation do not disappear when the narrower bands appear, the two structures may coexist at high temperatures or the first structure may evolve to a closely related but different crystal structure. From this example in Figure 3.3a, it is clear that visualizing 1D diffraction data as colormaps can quickly reveal primary regions of interest for structural characterization. The

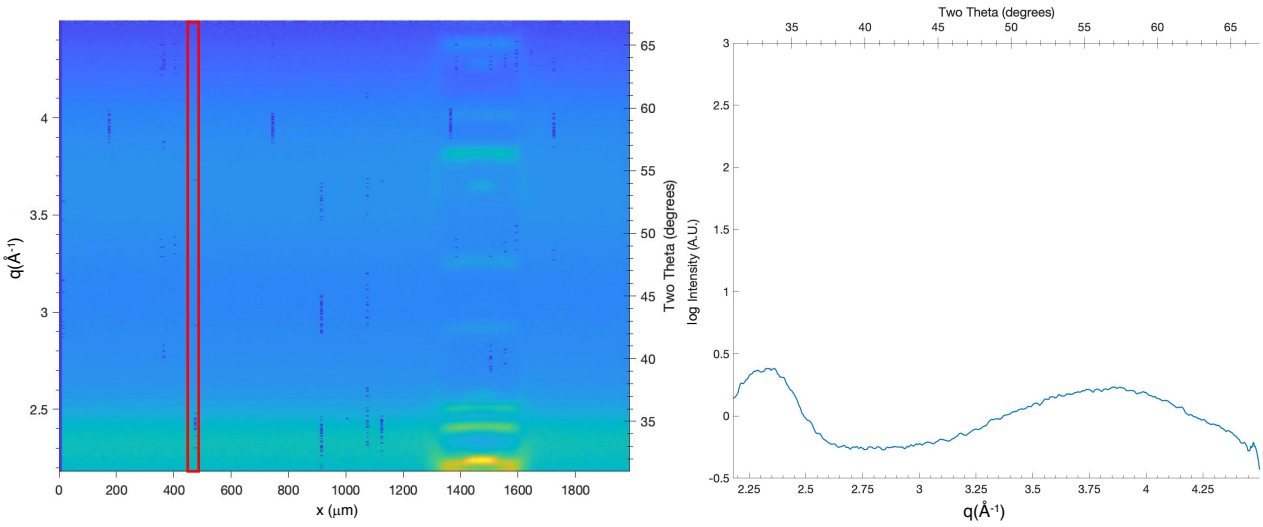

Figure 3.5 a) The colormap diffraction pattern for a 10 ms, high temperature stripe highlighting the amorphous region and b) the corresponding line scan. The amorphous region is characterized by diffuse scattering peaks and is visually distinct from the crystalline regions.

following sections will focus on analysis of three different IGZO structures evident in the colormap: the amorphous phase, the first crystalline structure, and the second structure.

3.5 Amorphous phase

The amorphous phase is characterized by the absence of sharp and distinct peaks. The amorphous structure, consisting of random arrangements of constituent atoms without long range order, results in few X-rays scattering constructively. An example colormap and line scan from the amorphous region of the film is shown in Figure 3.5. The two broad, weak peaks were fit with Gaussians at 2.34 ± 0.01 Å^{-1} and 3.85 ± 0.01 Å^{-1}. In previous studies, a characteristic amorphous peak of the m = 0.45 composition was located at 2.31 ± 0.01 Å^{-1} [28]. This roughly corresponds to the first peak in Figure 3.5b. Given the uniform intensity and location of the second diffuse peak in the colormap of Figure 3.5a, it is probable that this second peak can also represent scattering from the oxidized Si substrate. Figure 3.6 shows that the example

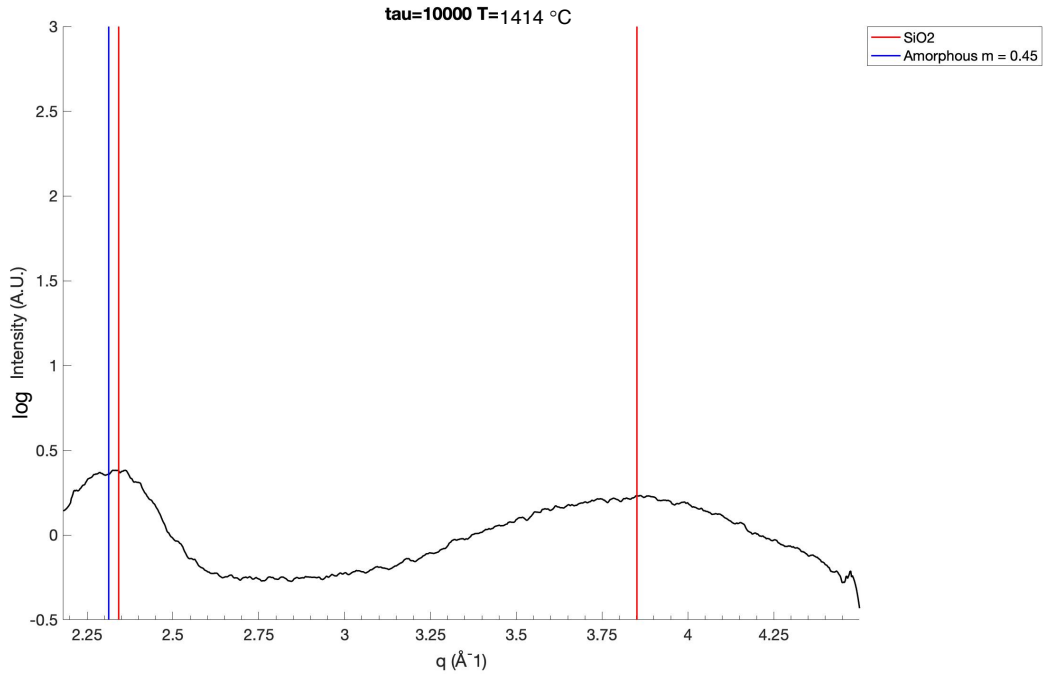

Figure 3.6 A line scan diffraction pattern for an example amorphous region at a 10 ms dwell, high temperature stripe overlaid with characteristic SiO_2 peaks (red) and a previously characterized amorphous m = 0.45 IGZO peak (blue).

amorphous region line scan shows overlap with the characteristic m = 0.45 amorphous peak and SiO_2 diffraction peaks [44]. However, for the purposes of this analysis, amorphous regions are identified by the absence of obvious characteristic crystalline peaks.

3.6 Crystal Structure I

The first onset of crystallization is clearly visible through the appearance of distinct scattering peaks extending across a significant width in the colormaps. An example colormap and line scan corresponding to the crystalline region is seen in Figure 3.7. The first crystallization event is defined by the appearance of the set of peaks shown in Figure 3.7b. These are eight peaks associated with this structure which consistently appear together; these peaks will be referred to as Structure 1. Structure 1 peaks were fit with Gaussians and peak centers were compared to previously studied structures of the $InGaO_3(ZnO)_m$ series. Given the film composition, analysis only considered structures in the m = 0 to m = 2 composition range of $InGaO_3(ZnO)_m$ (actual film would be m = 0.45 composition). Figure 3.8 shows this spectrum along with characteristic peaks for an m = 0 (In_2O_3:Ga_2O_3) structure, two m = 1 ($InGaO_3(ZnO)$) structures (the second with slightly larger lattice parameters), and an m = 2 structure [45]–[47]. The peaks overlap with

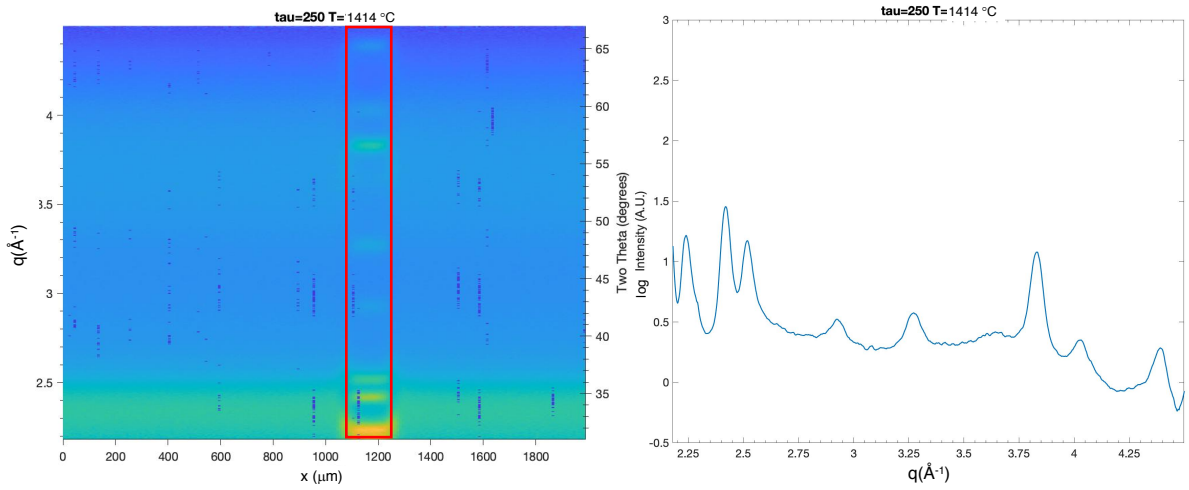

Figure 3.7 a) An example colormap for a stripe of 250 μs dwell and T_{peak} = 1414 °C with the Structure 1 transition region highlighted and b) an example line scan showing a crystalline region characteristic of Structure 1.

many characteristic peaks of the m = 0 and m = 1 structures, but only some of the m = 2 characteristic peaks. This is consistent with a non-integer m composition exhibiting characteristics of the two closest equilibrium structures.

3.7 Proposed Structure 1 Model and Formation Mechanism

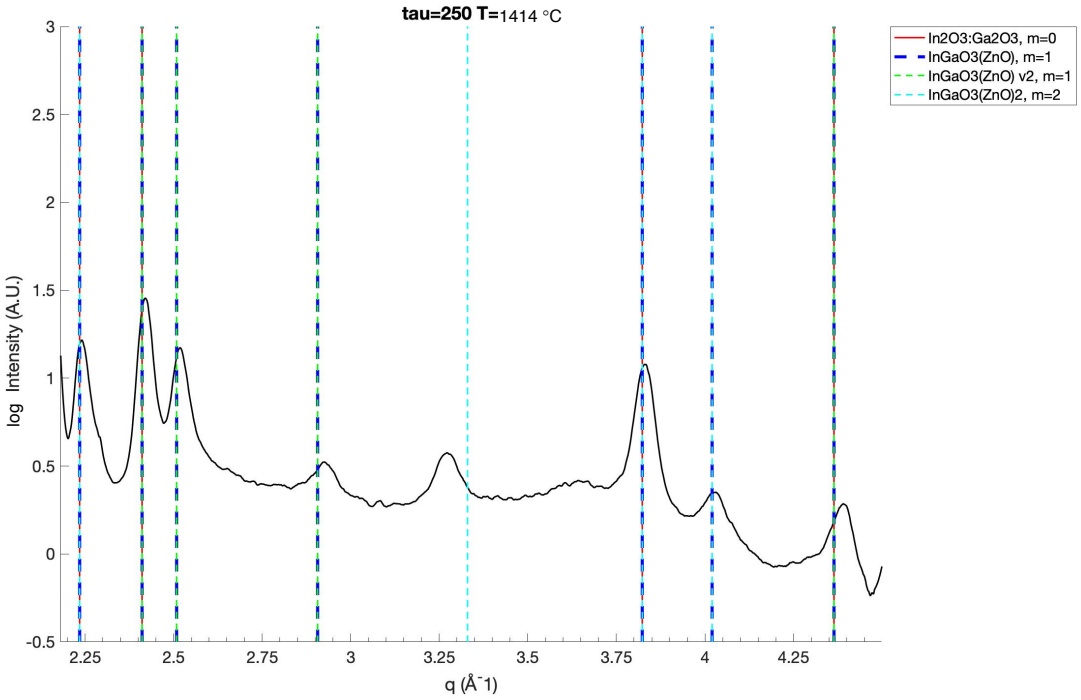

Figure 3.8 An example line scan of Structure 1 (250 μs and 1414 °C) overlaid with characteristic peaks of In_2O_3:Ga_2O_3, $InGaO_3(ZnO)$, $InGaO_3(ZnO)_2$.

As Structure 1 shares characteristics of both the m = 0 and m = 1 structures, it is likely a combination of the two structures. Figure 3.9a shows space-filling models of m = 0 and m = 1 structures for reference. In previous studies, non-integer m structures were found to phase segregate into alternating regions of the closest integer m structures [2]. While the diffraction patterns showing m = 0 and m = 1 peaks are consistent with this model, Structure 1 appears at anneal timescales as short as 250 μs and it is unlikely that would be sufficient time for phase segregation. Instead, we postulate that Structure 1 consists of an arrangement of random cations on the sublattice. A model of Structure 1 and a schematic of the proposed structure is

shown in Figure 3.9b. Annealing the amorphous phase initially allows atoms to adopt an ordered, lower energy structure without the full layered structure of either the m = 0 or m = 1

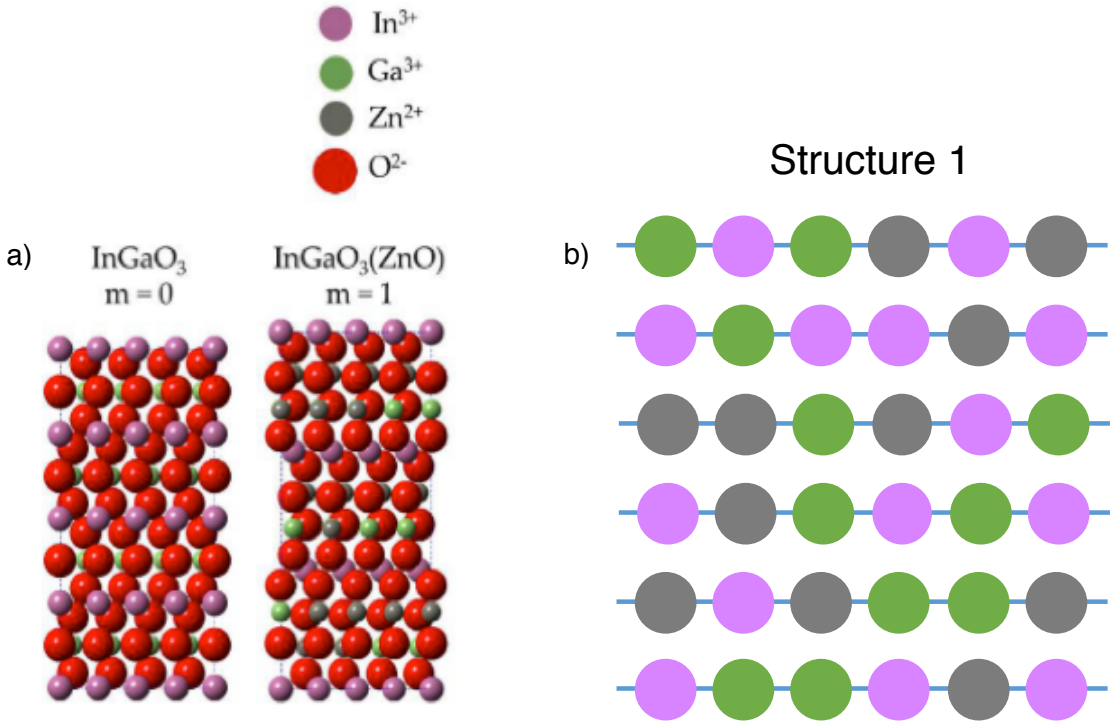

Figure 3.9 a) Space-filling models for $InGaO_3(ZnO)_m$ structures of m = 0 and m = 1 and b) a simplified model of Structure 1 showing cations In^{3+} (pink), Ga^{3+} (green), and Zn^{2+} (gray) as a disordered random alloy on the cation sublattice. Reference [2].

phase. Short dwell anneals, in particular, do not allow time for the full coalescence of In_2O_3 planes characteristic of m = 0 and m = 1 structures. This results in a high entropy, ordered structure that would have reflections consistent with the m = 0 and m = 1 phases. Assuming the model of a single peak temperature of 1414 °C, the onset crystallization temperature of Structure I was determined using the width of the transition region and Equation 3.1. The calculated onset crystallization temperature for Structure 1 was 1280 ± 50 °C.

3.8 Emergence of Crystal Structure II

The eight peaks corresponding to Structure 1 are found in the first crystalline region, for all conditions, and always appear as the first crystallization event. However, as seen in Figure 3.10, a second set of bands emerges at higher temperatures near the center of the laser stripe, indicating the formation of a second structure. Based on the conclusion that the actual temperature at the film did not increase above the Si substrate melting temperature of 1414 °C, this can be assumed to be the peak temperature of all the stripes and near the effective onset temperature of the second crystallization event.

Figure 3.11 shows a waterfall plot of diffraction line scans arranged by increasing dwell time. Short dwells (bottom) exhibit only Structure 1. However, as the dwell time increases, diffraction patterns begin to show additional peaks at approximate q-space locations of 2.58, 3.04, 3.64, and 4.27 $Å^{-1}$. These additional peaks consistently appear together and we identify the phase exhibiting these additional peaks as Structure 2. Examining stripes annealed with T_{peak} = 1414 °C , Structure 2 emerges for dwell times above 350-500 μs, suggesting that the formation mechanism of Structure 2 is time-dependent. At longer dwells in Figure 3.11, there is

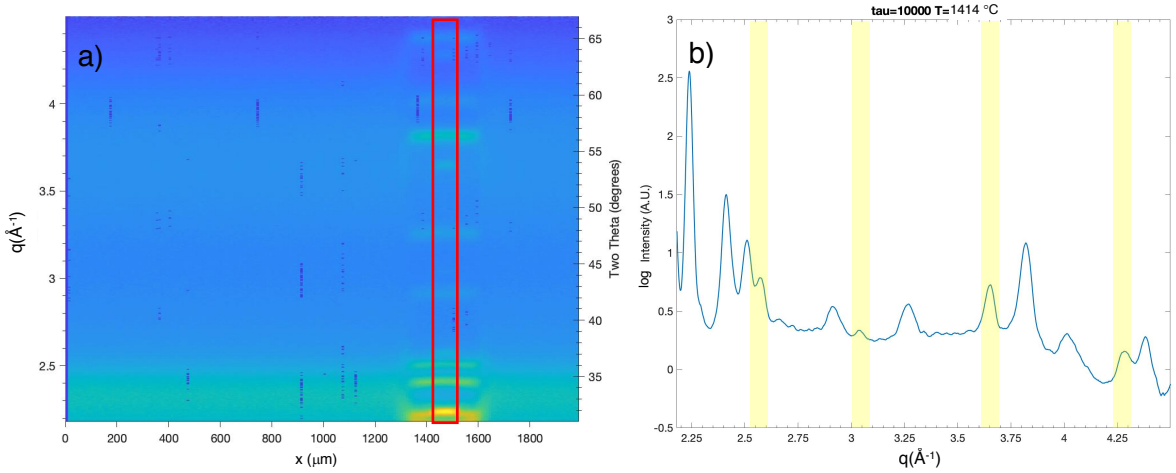

Figure 3.10 a) An example colormap for a stripe of 10 ms dwell and T_{peak} = 1414 °C with the Structure 2 transition region indicated and b) an example line scan showing a crystalline region characteristic of Structure 2. The characteristic peaks unique to Structure 2 are highlighted.

some evidence the structure may momentarily disappear before reemerging at the longest dwell. There are no apparent kinetic or thermodynamic explanations for a structure to disappear then reappear with increasing dwell time, and thus this result is thought to be an artifact of experimental limitations.

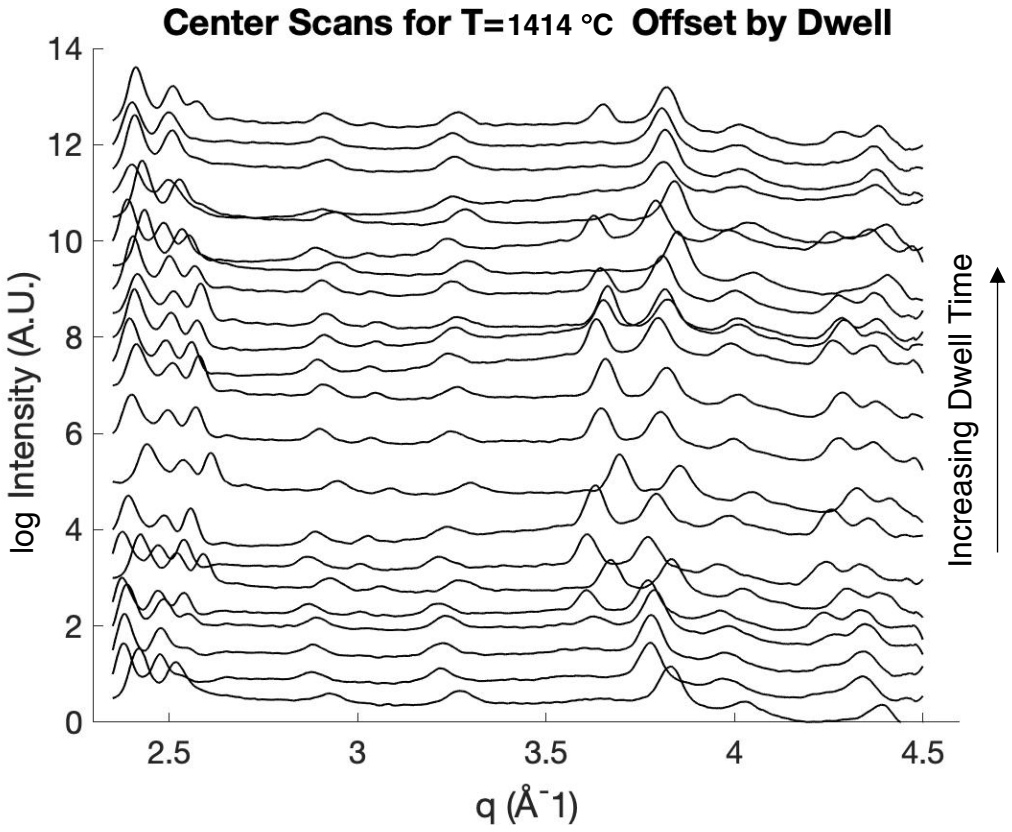

Figure 3.11 A waterfall plot for showing line scans at high temperature stripes with increasing dwell times along the y-axis. Short dwells show only Structure 1 characteristic peaks while Structure 2 peaks appear at dwells above 350 μs.

3.9 Crystal Structure II

The four additional peaks in Structure 2 were compared to m = 0, 1, and 2 diffraction patterns (Figure 3.12). The actual diffraction pattern is from a 2.5 ms dwell stripe. The new Structure 2 peaks fall close to m = 0, m = 1, and m = 2 characteristic peaks. However, Structure 2 only appears at longer timescales, implying that it is a lower energy structure with a higher degree of ordering. The dwell time is still likely too short to allow phase segregation into regions of m = 0 and m = 1 for this m = 0.45 composition.

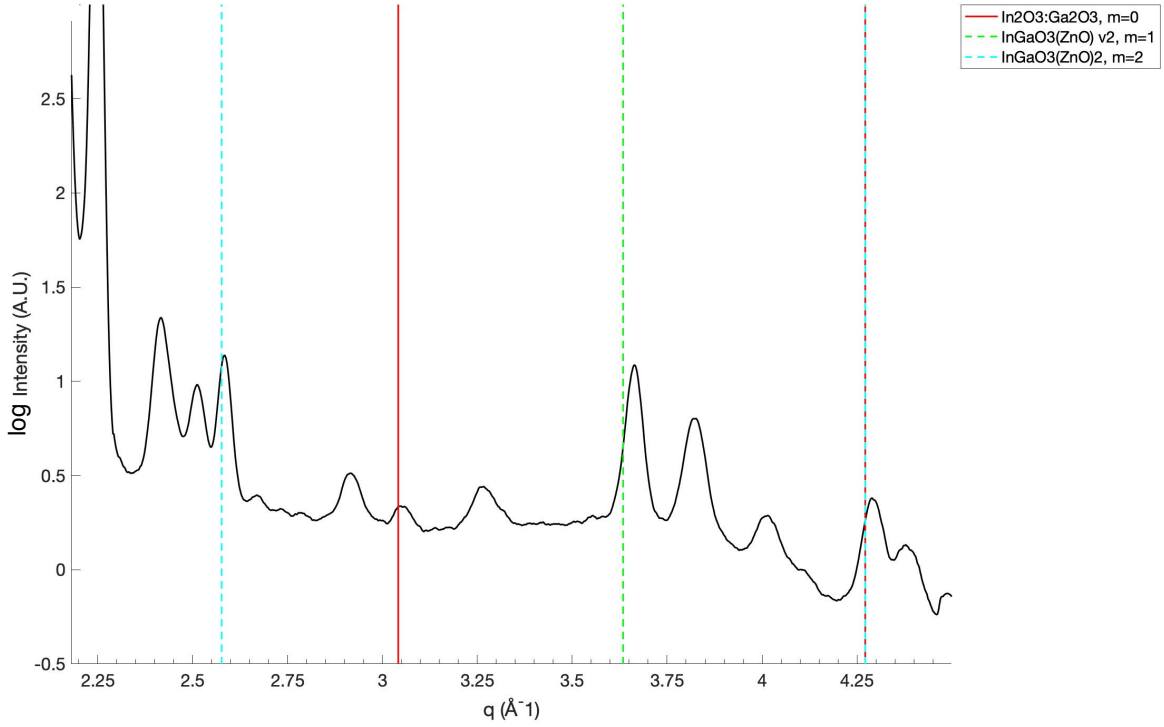

Figure 3.12 An example line scan of Structure 2 (2.5 ms at 1414 °C) overlaid with characteristic peaks of In_2O_3:Ga_2O_3, $InGaO_3(ZnO)$, $InGaO_3(ZnO)_2$.

3.10 Proposed Structure II Model and Formation Mechanism

We propose a model to explain these diffraction results that involves a hybrid of the m = 0 and m = 1 structure. Figure 3.13 shows the structural evolution of the $InGaO_3(ZnO)_m$ series. As noted earlier, the basic structure is In_2O_3 planes that enclose random alloys (Ga, Zn)O_x. With increasing m, the separation between In_2O_3 planes increases to contain m + 1 Ga/Zn layers. The m = 0 structure shows In_2O_3 planes separated by one Ga layer while in the m = 1 structure, In_2O_3 planes are separated by two disordered Ga/Zn layers. We propose that Structure 2 consists of ordered In_2O_3 planes with statistically distributed separation distance of one or two layers of disordered Ga/Zn layers. This proposed model is consistent with the appearance of m = 0 and m = 1 peaks. Figure 3.14 shows this proposed model as cation planes. Structure 2

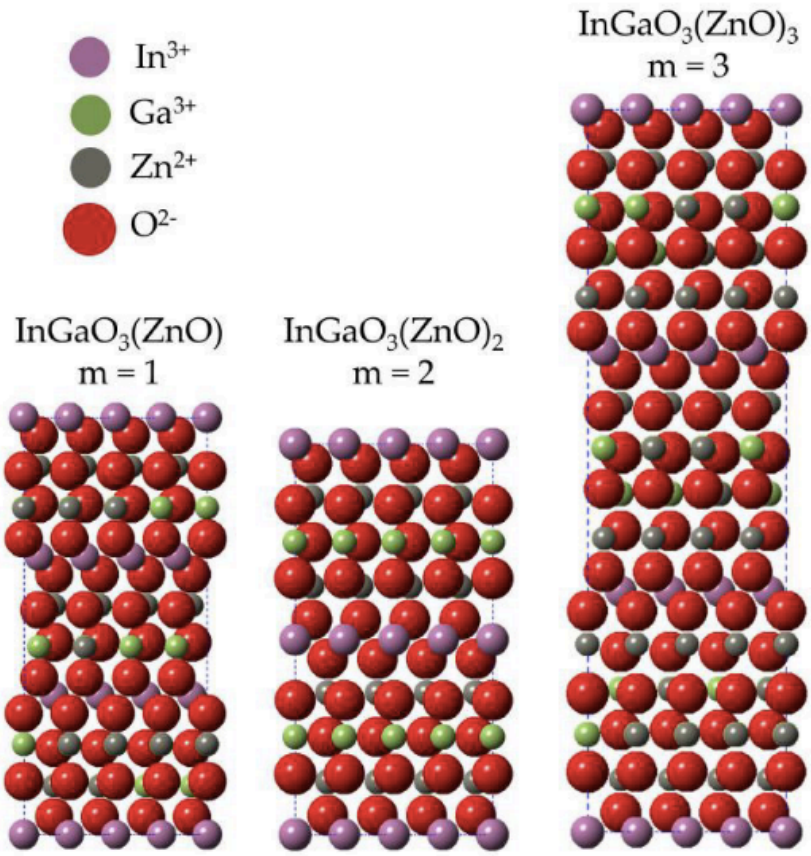

Figure 3.13 Space-filling models for the $InGaO_3(ZnO)_m$ series of m = 1-3 showing the m + 1 Ga/Zn layers separating In_2O_3 planes. Reference [2].

would evolve from Structure 1 in this model at longer dwells and higher temperatures as there is sufficient time to order and coalesce the In_2O_3 into planes. Ga and Zn cations remain randomly dispersed in distorted tetrahedra coordination in the intervening layers. The second crystallization transition from Structure 1 to Structure 2 sacrifices the high entropy configuration of Structure 1 for a lower energy, more ordered Structure 2.

Assuming the model of a single peak temperature of 1414 °C, the onset crystallization temperature of Structure II could be determined using the width of the second transition region as shown in Figure 3.10a and Equation 3.1. The calculated onset crystallization temperature for Structure 2 was 1395 ± 15 °C.

3.11 X-ray Characterization Conclusions

X-rays were used to study the structural evolution of an $InGaO_3(ZnO)_m$ alloy at m = 0.45 as a function of laser spike annealing conditions. X-ray diffraction measurements from 115 anneal stripes at T_{peak} = 1414 °C and dwell times ranging from 250 μs to 10 ms. Crystallization was observed across all of these conditions. As deposited, the $In_2Ga_2ZnO_7$ film was amorphous. Two distinct crystalline transformations were observed. The first appearing under all conditions while the second appeared only at high temperatures and for dwell times longer than 350 μs. The first structure has a crystallization onset temperature of 1280 ± 50 °C and we hypothesize its structure consists of a random composition cation sublattice. This model is consistent with diffraction data showing peaks characteristic of the m = 0-2 phases of $InGaO_3(ZnO)_m$. The second crystal structure crystallized at higher temperatures with an estimated onset temperature of 1395 ± 15 °C . We similarly hypothesize that this second structure consists of In_2O_3 planes separated by one or two Ga/Zn layers, consistent with observations of m = 0-2 peaks in the diffraction data.

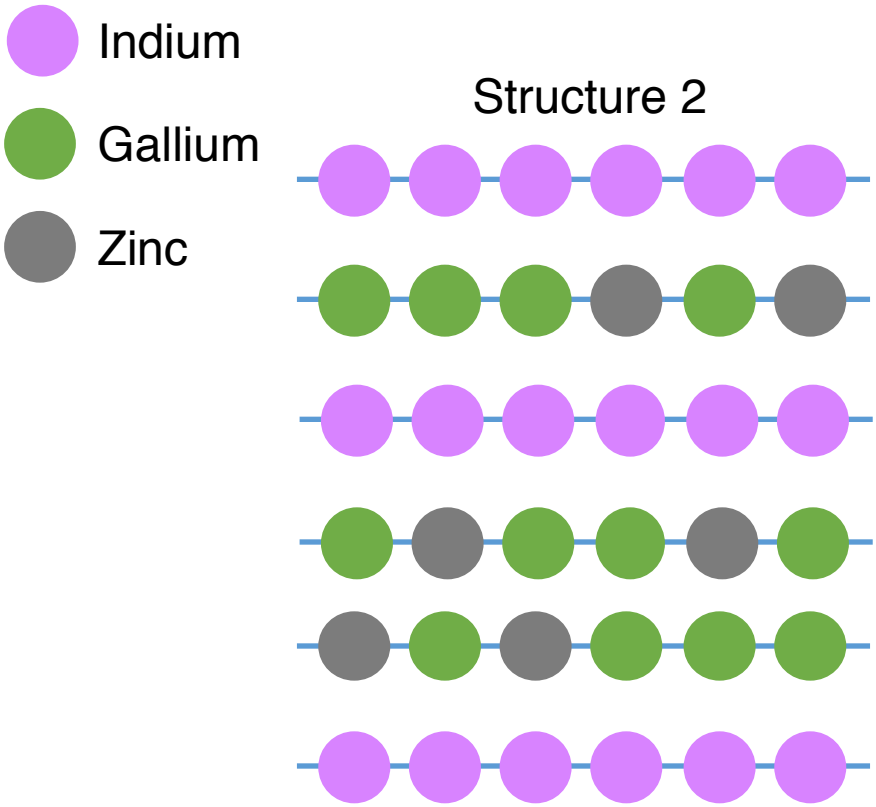

Figure 3.14 A simplified model of Structure 2 showing In_2O_3 planes separated by 1-2 disordered Ga/Zn layers.

CHAPTER 4

OPTICAL REFLECTANCE STRUCTURAL CHARACTERIZATION

4.1 Optical Characterization Overview

Optical reflectance measurements were implemented in this work as a potential technique to rapidly identify structural transition by discontinuous shifts in the optical properties of a film. Optical properties are determined by both the index of refraction n and the thickness t, which together can be described as the optical thickness nt. Discontinuous nt across an annealed region would likely indicate a structural transition such as crystallization while continuous changes would indicate densification as a result of annealing. This experimental setup, as described in section 2.6.3, occurs on a tabletop set up, takes very little calibration time between samples, is completely automated, and can complete in its measurement of all LSA stripes in just under three days. It is also a simple, non-destructive, and fast and has tremendous potential for rapid identification of regions of interest before more detailed structural evaluation via high-energy synchrotron X-ray diffraction. In this work, we evaluated this optical reflectance technique using an X-ray characterized $In_2Ga_2ZnO_7$ film, analyzing the observed changes in optical thickness and comparing with known regions of structural transition determined from the X-ray analysis.

4.2 Optical Data Processing

Optical reflectance was collected for wavelengths from 340-1026 nm across a 1 mm region centered on each LSA stripe. The reflectance of an opaque, non-reflective surface was measured for a standard of no reflectance (blank) and the reflectance of a mirror surface was measured to establish 100% reflectance (mirror). The raw, blank, and mirror optical reflectance

data is first smoothed using a low-pass Savitzky-Golay smoothing function in Matlab. The smoothed raw, blank, mirror, and reflectance data are shown in Figure 4.1.

The reflectance data is then normalized using the formula given by Equation 2.3. As with X-ray data, the reflectance for a series of measurements across a larger stripe are combined in an image. Figure 4.2 shows these 101 smoothed and normalized reflectance scans of a high temperature, long dwell stripe stitched together into an reflectance image of a stripe. Changes in the spectra are apparent near the center of the image corresponding to the annealed region. Figure 4.2b also shows these images for all annealing conditions arranged by their position on

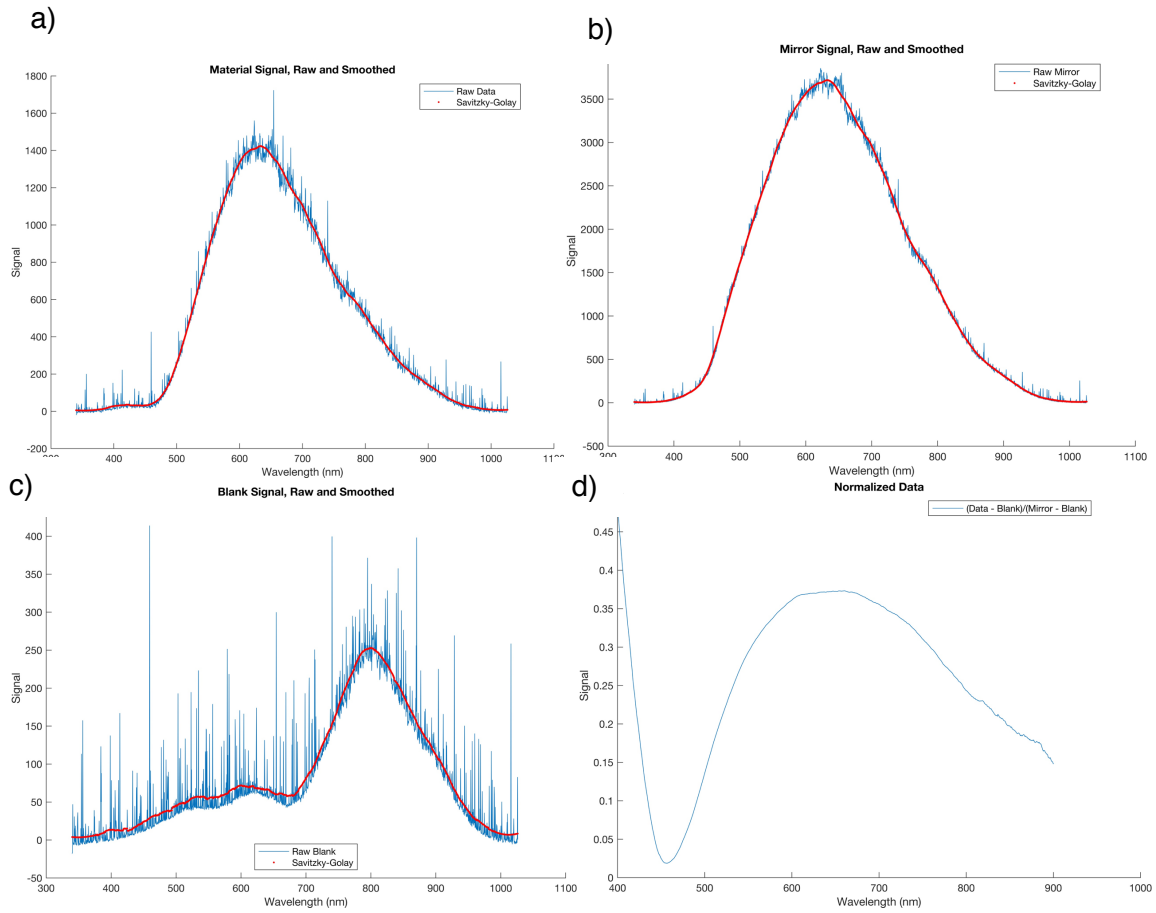

Figure 4.1 a) Example scans of raw reflectance data and b) mirror and c) blank data showing the reflectance profile before (blue) and after (red) passing through a Savitzky-Golay smoothing function and d) showing the resulting smoothed and normalized reflectance data. Reflectance scans are plotted as reflectance signal by wavelength.

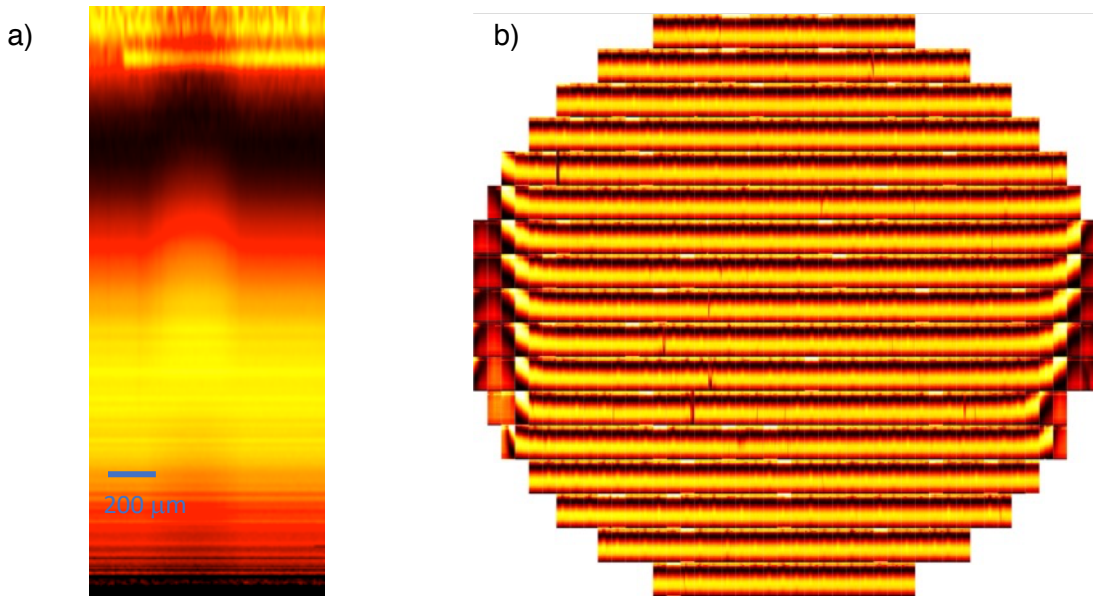

Figure 4.2 a) Example reflectance image of a stripe composed of 101 individual reflectance scans plotted vs. distance across the stripe and b) the reflectance images for each stripe arranged by their position on the wafer where the bottom of the arrangement corresponds to the wafer flat. Images at the edge of the wafer show anomalous reflectance behavior due to greater variations in film thickness at the edges of the sample.

the sample wafer. The rapid changes on the left and right arise from thinning of the film near samples clips used during deposition.

4.3 Comparison of Optical and X-ray scans

Both optical reflectance and X-ray measurements quantify changes in sample structure, and hence optical reflectance images and X-ray colormaps of the same stripe may correlate. The transition near the center of the optical reflectance images may correspond to the crystallization observed in the X-ray colormaps. The width of the optical transition and the width of the crystallization region were compared for several stripes. Figure 4.3 compares the images for a stripe annealed at T_{peak} = 1414 °C and for a dwell time of 10 ms. The width of the reflectance image transition region is estimated to be 400 μm while the width of the crystalline region on the X-ray colormap is only 280 μm. Several optical reflectance images and X-ray colormap pairs were evaluated and the width of the optical transition region was consistently larger than the

crystallized region. This suggests that, while the optical transition region does reflect a change in the optical thickness, this does not directly correspond with crystallization. It is likely that optical reflectance changes are a result of film densification in the annealed regions.

4.4 Annealed Region Reflectance Shift

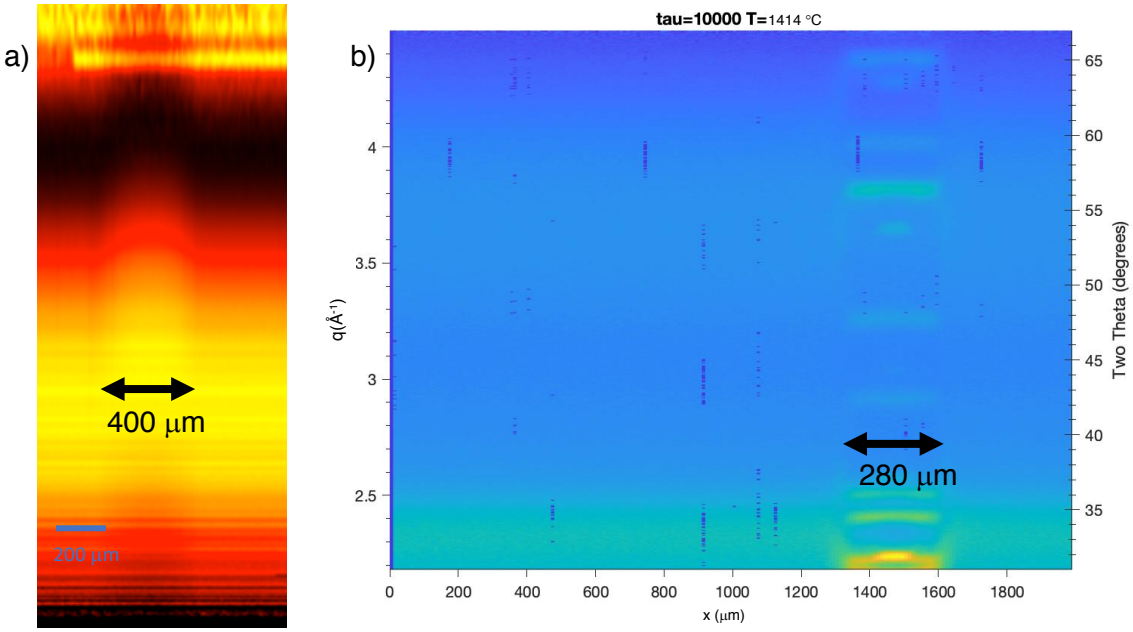

Figure 4.3 a) The optical reflectance image and b) X-ray colormap of a stripe annealed at 1414 °C with a 10 ms dwell. The widths of the transition regions in the optical image and X-ray map are estimated to be 400 μm and 280 μm respectively, suggesting a discrepancy in the origins of the observed transition regions. While the X-ray map transition region is consistent with crystallization, the optical transition region could be an effect of densification.

Detailed changes in the optical reflectance scans between the edge (unannealed) and near the center stripe (highest temperature) were investigated to understand the optical response to annealing. Figure 4.4 shows the reflectance spectrum in this comparison for a stripe annealed at 1414 °C with a 10 ms dwell. There is a shift toward lower wavelengths with increased annealing. The shift to lower wavelengths is consistent with a decrease in the optical thickness

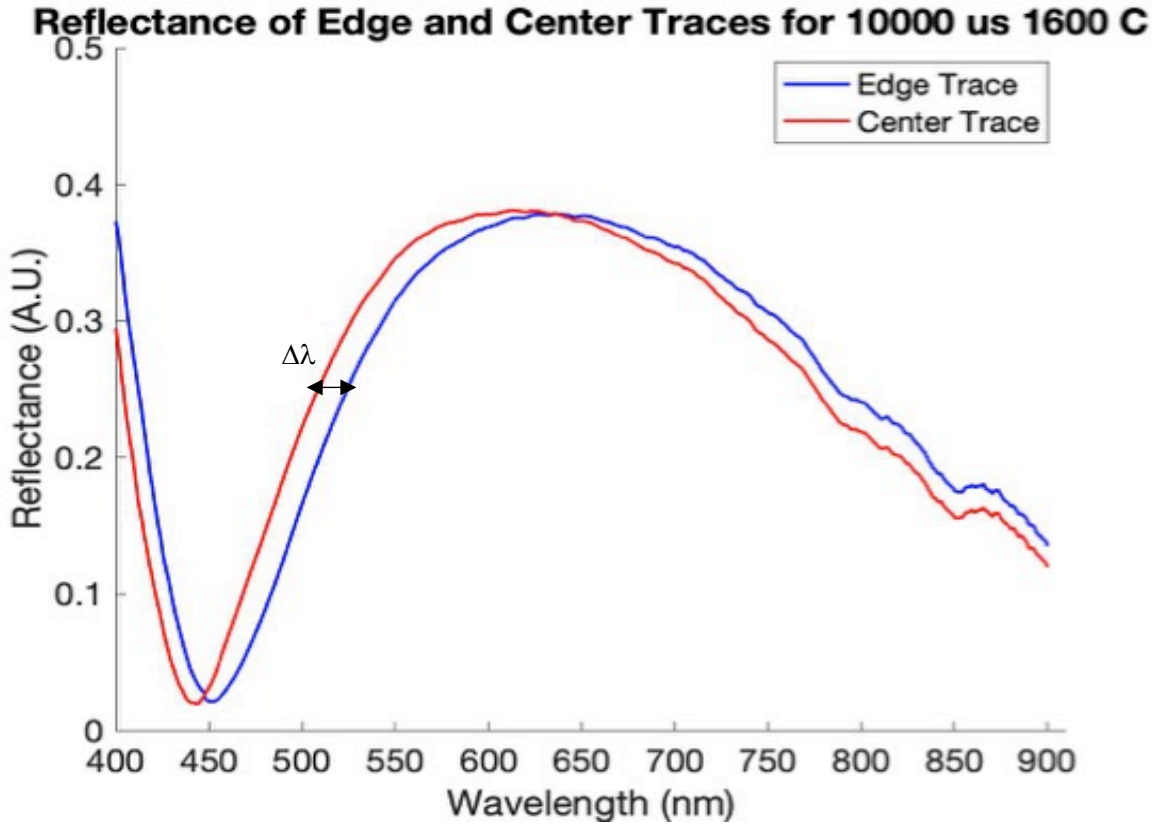

Figure 4.4 Optical reflectance scans from as-deposited, unannealed areas (blue) and at the center of the stripe, in the annealed region (red) for a stripe annealed at 1414 °C and 10 ms. The reflectance data shifts to lower wavelengths with annealing and is consistent with densification.

nt. We have confirmed through EDS (A.1) that the film composition did not change with annealing and, based on the X-ray studies, we do not believe that any structural changes are large enough to substantially change the index of refraction. This is further evidenced by the lack of any discontinuities in the optical data at the onset of crystallinity. Consequently, the reflectance shift to lower wavelengths indicates primarily a reduction in film thickness due to densification.

4.5 Quantification Wavelength Shift

The reflectance shift between the peak anneal temperature and the corresponding unannealed areas was quantified as wavelength shifts at a reflectance value of 0.3, in the range of 450-550

nm. This shift is shown as $\Delta\lambda$ in Figure 4.4 (the $\Delta\lambda$ data for two dwells and target temperatures

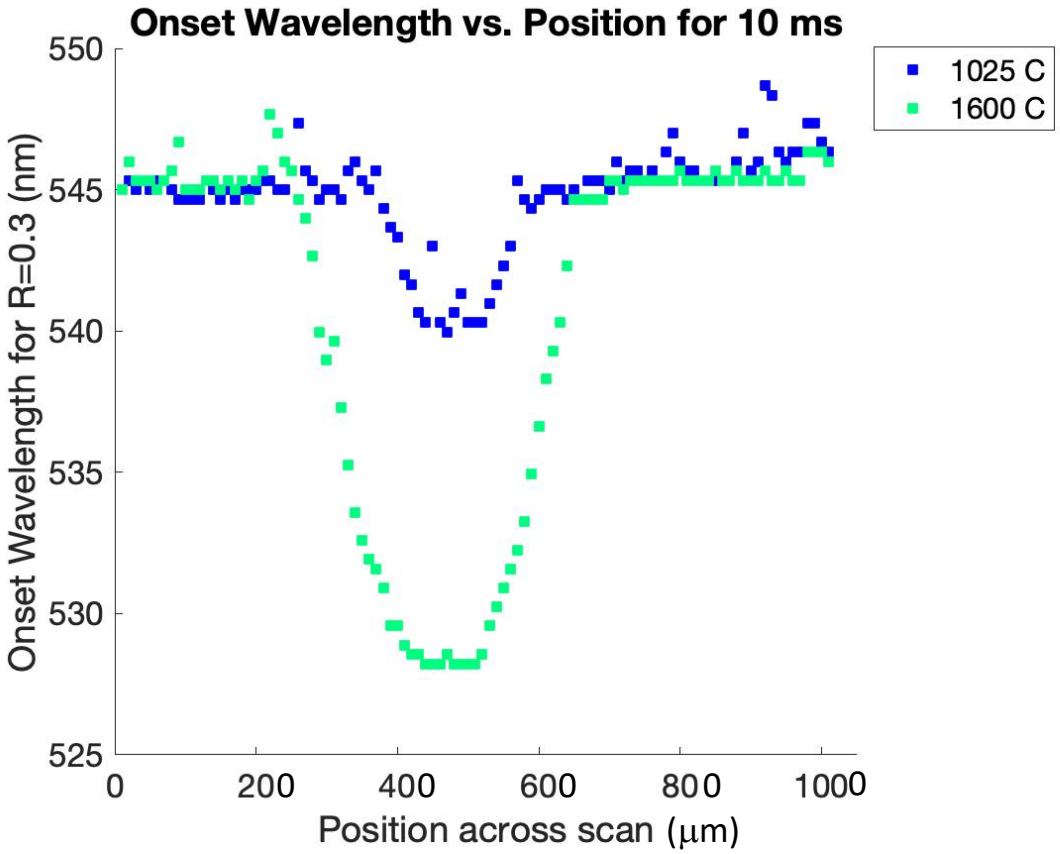

Figure 4.5 Onset wavelength for a reflectivity of 0.3 by position for two 10 ms dwell stripes annealed, one at targeted temperatures of 1025 °C and 1600 °C. The maximum wavelength shift between unannealed and annealed regions is the difference between the onset wavelength in the unannealed region and the onset wavelength in the stripe center.

are shown in Figure 5) . Figure 4.5 shows wavelength where the reflectivity equals 0.3 as a function of position for two 10 ms stripes, one annealed at 1025 °C and the other annealed at a target temperature of 1600 °C. For both stripes, the onset reflectance crosses 0.3 at 545 nm in unannealed material. This wavelength decreases as the scan approaches high temperature annealed material at the center of the stripe before increasing again as the anneal temperature drops. The maximum wavelength shift ($\Delta\lambda$) was determined in this fashion.

4.6 Effect of Anneal Conditions on Wavelength Shift

As the optical reflectance measured all stripes, the range of targeted peak temperatures includes 1000-1600 °C for dwells of 250 μs – 10 ms, though we believe all targeted temperatures above 1414 °C are actually just 1414 °C. The data as a function of target temperature, color-coded by dwell time, are shown in Figure 4.6a. As expected, $\Delta\lambda$ increases monotonically with temperature, indicating an increasing densification of annealed regions with higher temperatures. The rate of increase is nearly linear with targeted peak temperature up to 1400 °C, with a decrease in slope above 1400 °C . This change at 1400 °C is likely an artifact of the onset of Si melt capping actual temperatures to 1414 °C as hypothesized in section 3.3. Below 1400 °C, the increase in $\Delta\lambda$ with temperature is consistent with our densification model. While there was no obvious change in the reflection data at the 1280 $\pm$ 50 °C crystallization threshold, further analysis work may be able to identify more subtle changes that would provide evidence of crystallization events.

We can also examine the role of dwell in Figure 4.6a. There is a consistent trend at long dwells exhibiting a smaller $\Delta\lambda$ compared to short dwells. This effect of dwell on $\Delta\lambda$ is more clearly visible in Figure 4.6b, where $\Delta\lambda$ is plotted as a function of dwell time with color-coding of the targeted peak anneal temperature. The highest temperature stripes still consistently exhibit the $\Delta\lambda$. But for dwell time, $\Delta\lambda$ initially increases with dwell up to 650 μs before the gradually decreasing. The initial increase is restricted to only the shortest dwells and may be an artifact of the specific data. In the case of the apparent decrease in delta with dwell, we hypothesize within the model of densification that this trend is evidence of structural relaxation. In this model, the film densifies to the greatest degree at high anneal temperatures and midrange dwell times.

This extent of densification may be beyond equilibrium levels and may be metastable. At longer

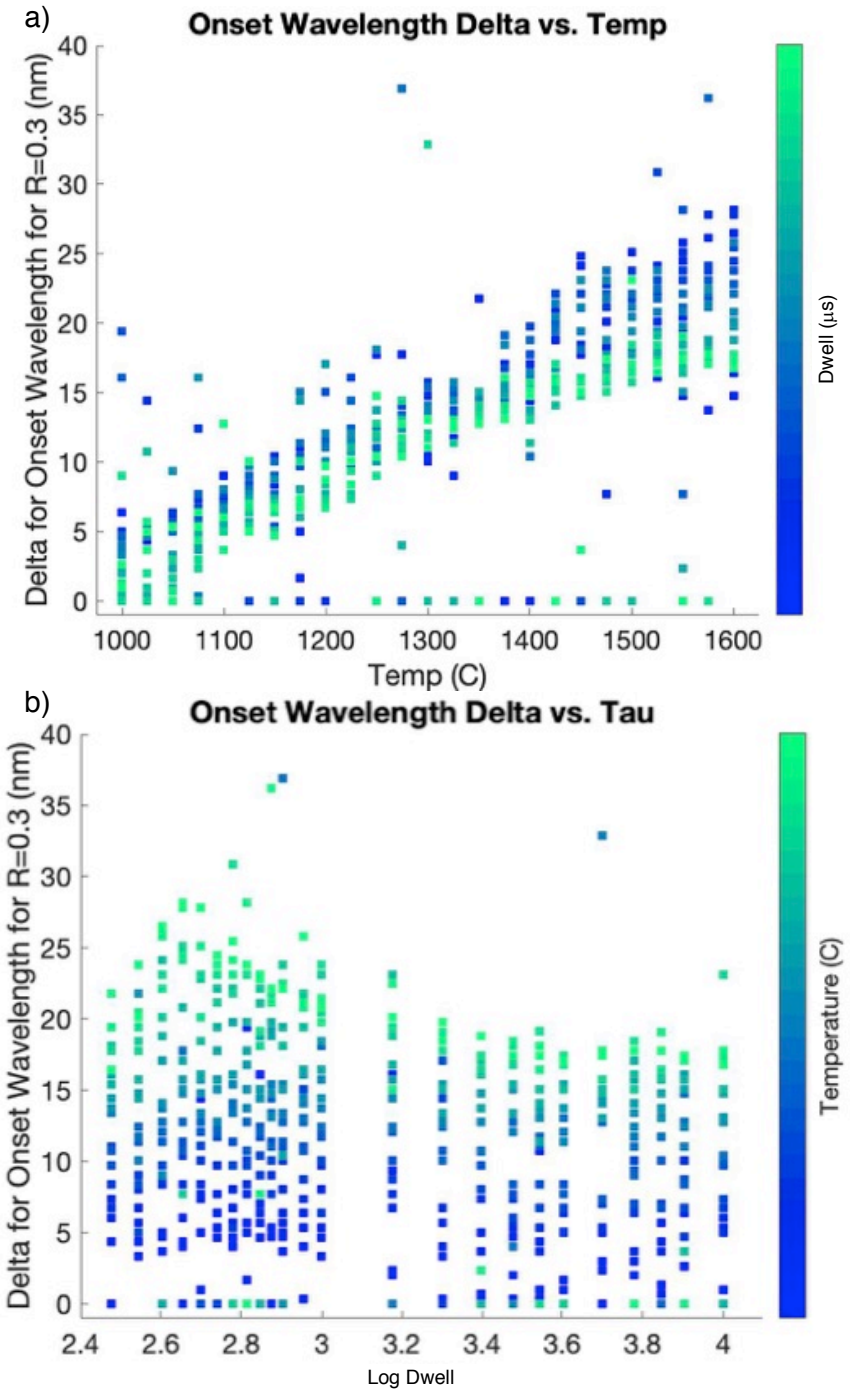

Figure 4.6 a)The delta in onset wavelength vs. targeted peak anneal temperature and color-coded by dwell time. The shift, or delta, shows a steady increase with peak anneal temperature. b) Delta vs. dwell time color-coded by temperature. Delta initially increases with dwell up to 650 μs before gradually decreasing with dwell.

dwells, the film initially assumes this level of densification but now has sufficient time to relax into a more stable dense structure.

4.7 Optical Characterization Conclusions

We implemented a simple, non-destructive technique to measure the optical reflectance of $In_2Ga_2ZnO_7$ films heated by millisecond laser spike annealing. This technique was pursued to determine if optical reflectance could be used to rapidly identify region of structural transition or crystallization based on changes in optical behavior. We identified transitions in the optical reflectance but found that these do not correspond with crystallization events. We suggest that these optical changes reflect film densification. Quantitative measurements of optical changes were shown to scale with temperature and were consistent with densification. An unusual shift with dwell was also observed which may indicate structural relaxation.

CHAPTER 5

CONCLUSIONS & FUTURE WORK

5.1 Conclusions

As flat panel displays become increasingly large with ever higher resolutions, the devices and materials required by these displays must also evolve to enable next generation technology demands. In the past decade, alloys in the IGZO (In-Ga-Zn-O) have shown great potential to replace existing forms of Si as the active semiconductor in thin film transistors. Amorphous IGZO exhibits large area uniformity, a controllable carrier concentration and reasonable carrier mobility. More recently, crystalline IGZO has been developed to address the electrical instabilities associated with the defects in amorphous IGZO, while still maintaining high area uniformity and exhibiting an even lower off-state current in devices. Thus, a great deal of interest has been directed at studying the structure and crystallization mechanisms of IGZO alloys. This work considers the formation mechanisms and structures of $In_2Ga_2ZnO_7$ films crystallized by millisecond laser spike annealing.

In this study, RF magnetron sputtering was used to deposit $In_2Ga_2ZnO_7$ films at room temperature. The as-deposited amorphous films were annealed at target peak temperatures of 1000-1600 °C and dwell times of 250 μs - 10 ms using lateral gradient laser spike annealing with a 10.6 μm CO_2 source laser. The annealed films were then studied using by X-Ray diffraction (WAXS) and white light optical reflectance (400-100 nm). Crystallization was observed for all studied stripes in the 1400-1600 °C target peak anneal temperature range; however, the lack of correlation between crystallization region width and peak temperature suggests that sample and laser decoupled above the Si substrate melting temperature of 1414

°C and all stripes annealed with target temperatures above Si melt were effectively annealed at 1414 °C.

Two distinct crystalline structures were observed. We determined that the onset crystallization temperature for the first structure was 1280 ± 50 °C. This structure was characterized by comparing its diffraction pattern to those of nearest integer structures m = 0 and m = 1. Substantial overlap was observed with both integer structures, as would be expected for an m = 0.45 film. We propose a model consisting of a crystallized layer structure but with random In, Ga, or Zn on the cation sublattice. This is in contrast to the equilibrium phase where In_2O_3 orders further into segregated c-axis planes.

The second crystal structure was observed at the highest anneal temperature with additional diffraction peaks appearing with for dwells longer than 350 μs. The onset crystallization temperature for this structure was found to be 1395 ± 15 °C. The diffraction patterns of this second crystal structure matched expected peaks of the m = 0, m = 1, and m = 2 phases. We hypothesize that Structure 2 consists of a superlattice of In_2O_3 planes separated by a varying number of disordered Ga/Zn layers. Structure 2 only appears at longer dwells where there is sufficient time for In_2O_3 planes to coalesce with alternating separation distance of m + 1 Ga/Zn subplanes.

Optical reflectance was also used to identify structural changes during annealing based on the optical thickness, nt. Optical reflectance data indeed showed significant changes, but these changes began to occur at temperatures significantly below crystallization as measured by X-ray analysis. The observed optical transitions appear to reflect primarily densification. Densification was quantified as a shift in spectral behavior. This shift was found to increase almost linearly with peak annealing temperature. Surprisingly, the greatest changes in optical

properties occurred at intermediate dwells, indicating that the details of relaxation are time-dependent.

5.2 Future Work

There are still many unanswered questions about the crystallization conditions, kinetics, and mechanism for structures in $In_xGa_{1-x}O_3(ZnO)_m$ composition space. This study only explored the behavior of one of the non-integer m compositions, about which even less is known. More integer and non-integer compositions can be studied more efficiently by the co-sputtering of In_2O_3 and ZnO targets to achieve a tunable composition gradient. This technique already realized success in previous studies and is being employed in our group's current work [2], [34].

While lgLSA remains a novel and high-throughput approach for annealing films over a range of conditions, we still lack accurate information about the actual temperature experienced at the film during annealing. Future efforts should focus on developing *in situ* temperature calibrations or identifying a substrate material that can be used for universal substrate temperature calibrations.

Optical reflectance was implemented in this study with the possibility of rapidly identifying regions of crystallization. While this work found that the most obvious transitions in the optical reflectance data do not correspond to the crystallization transitions seen in X-ray data, there may be more complex signs of crystallization hidden in the reflectance signal. Further work deconvoluting the optical reflectance signal is needed to optimize this technique.

Though recent works and this work have focused more on structural characterization of crystalline $In_xGa_{1-x}O_3(ZnO)_m$, the electrical characteristics of these alloys are extremely relevant to its potential for use in TFTs. Previous work focused on developing a technique to study the electrical behavior as a function of annealing conditions using microdevices fabricated on laser

spike annealed regions. Process improvement and automated electrical measurement equipment will be needed to advance work in this direction. Comprehensive approaches that utilize structural and electrical characterization to optimize the properties of the ternary alloys are needed to expand the use of IGZO in real world applications.

APPENDIX

OTHER CHARACTERIZATION TECHNIQUES

Other Characterization Techniques

Several different techniques were explored to further characterize the structural and electrical properties of IGZO.

A.1 Composition analysis

Composition analysis was performed on an IGZO film to determine whether the deposited composition matched to the target composition. Energy dispersive spectroscopy was used to estimate relative quantities of the elemental constituents by Energy Dispersive Spectroscopy (EDS).

EDS involves the interaction of an electron beam with the surface of a material stimulating the emission of characteristic x-rays. Characteristic x-rays are emitted from the sample when an outer-shell electron decays to an inner-shell vacancy created by the incoming electron beam. The energy difference between the inner-shell vacancy and the outer-shell electron is released as an X-ray. Each X-ray energy is characteristic to an atomic species in the material, thus the X-ray energy measured by the EDS detector can be used for elemental analysis. A Leo 1550 FESEM with a Bruker SSD X-ray detector was used in this experiment. Esprit Microanalysis software was used to collect and measure X-ray spectra and automatically identify elements present by their peaks. The software was also used to automatically determine elemental quantity by atomic percent based on relative peak height.

Normalized amounts of In, Ga, Zn, and O for non-annealed film and three anneal conditions are given in Table A.1. The anneal dwell times and targeted peak temperatures for the three stripes are 10 ms, 1600 °C; 10 ms, 1500 °C; and 250 μs, 1500 °C. The oxygen signal

is not reflective of the oxygen content in the film as the SiO_2 layer under the IGZO will also contribute to the total oxygen signal. These results would imply an IGZO composition of $In_{1.41}Ga_{1.86}ZnO_x$. This is relatively similar to the target composition of $In_2Ga_2ZnO_7$.

Table A.1 A list of relative elemental percentages of Oxygen, Zinc, Gallium, and Indium in an $In_2Ga_2ZnO_7$ film before and after LSA as measured by EDS. Three stripes were laser spike annealed at the following dwell times and targeted peak temperatures: 10 ms, 1600 °C; 10 ms, 1500 °C, 250 μs, 1500 °C.

Element	Pre-anneal	Stripe 1 Center	Stripe 2 Off-stripe	Stripe 2 Center	Stripe 3 Off-stripe	Stripe 3 Center
Oxygen	23.65	22.93	24.16	24.05	23.50	23.63
Zinc	0.97	0.69	1.00	0.89	0.76	0.76
Gallium	1.61	1.19	1.71	1.60	1.30	1.31
Indium	1.37	0.91	1.42	1.33	1.08	1.01

A.2 Raman Spectroscopy

Raman spectroscopy is an optical characterization technique that can be used access information about a material's composition and crystallinity by observing vibrational and rotational modes in a crystal lattice. In Raman spectroscopy a laser light of a single wavelength illuminates a sample, interacts with molecules in the material, and excites electrons into a temporary higher virtual energy state. The excited electrons relax to a lower energy state and scatter back this light which is collected by the detector. A majority of the time, the incoming light is elastically scattered by the sample and the reflected light has the same magnitude as the incoming light. This is called Rayleigh scattering. However, a small fraction of incoming light can be inelastically scattered, meaning the emitted energy differs from the incoming energy. The energy shift between the incoming and emitted light is measured and analyzed to give information about the material's lattice vibration modes, or phonons.

In many materials, these phonon modes can be analyzed to estimate the carrier density. Raman spectroscopy was explored in hopes of quantifying the carrier concentration in IGZO as a function of LSA annealing conditions. Additionally, the Raman spectra output of scattering intensity by phonon frequency can provide information about changes in crystalline quality or composition.

A Renishaw InVia Confocal Raman microscope was used to analyze the same IGZO sample referenced in Chapter 2. Using a 488 nm laser source, a light probe of 1 μm diameter was focused on the sample and spectra were collected in four different approximate locations: off the laser stripe in an unannealed region, on the edge of the stripe, midway between the edge and center of the stripe, and at the center of the stripe. Spectra were compared to screen for differences between the four sampled locations. Unfortunately, spectra from the four different locations looked identical, with no observed changes in peak intensity or position that would indicate change in crystallinity or composition as a function of annealing.

A.3 Electrical Characterization

In 2018, IGZO films were fabricated in van der Pauw structures with the intent of measuring the films' conductivity, sheet carrier density, and Hall mobility.

Amorphous thin film samples of $In_2Ga_2ZnO_7$ were deposited onto thermally oxidized, low-doped, p-type Si substrates (10-20 Ω-cm). Films were deposited using the same sputter system, target, gases, pressure, and temperature as mentioned in Chapter 2. An RF power of 120 W was applied over a 19 minute deposition to achieve approximately 50 nm thick amorphous films.

A.3.1 Van der Pauw Device Construction

Following deposition, a passivating SiO_2 film approximately 30 nm thick, was deposited using an Oxford 100 PECVD system to protect the surface of the active material. This passivation film was deposited at 200 °C to minimize thermal effects in a 20 sccm SiH_4, 2500 sccm N_2O gas environment at 1800 mTorr. The RF power was held at 50 W for the 14 second deposition.

Samples were photolithographically patterned to form spatially resolved van der Pauw structures, as schematically shown in Figure A.1. The active layer was etched with a dilute 5% HCl solution for two minutes. Each device consisted of four 50 μm contact pads contacting a 6 x 6 μm active van der Pauw area. Devices were combined into rows with each device row displaced 5 μm to allow profiling of properties across a temperature profile developed during the laser annealing. After patterning, samples were annealed at 350 °C with 7 sccm N_2 for 30 minutes in a quartz tube furnace.

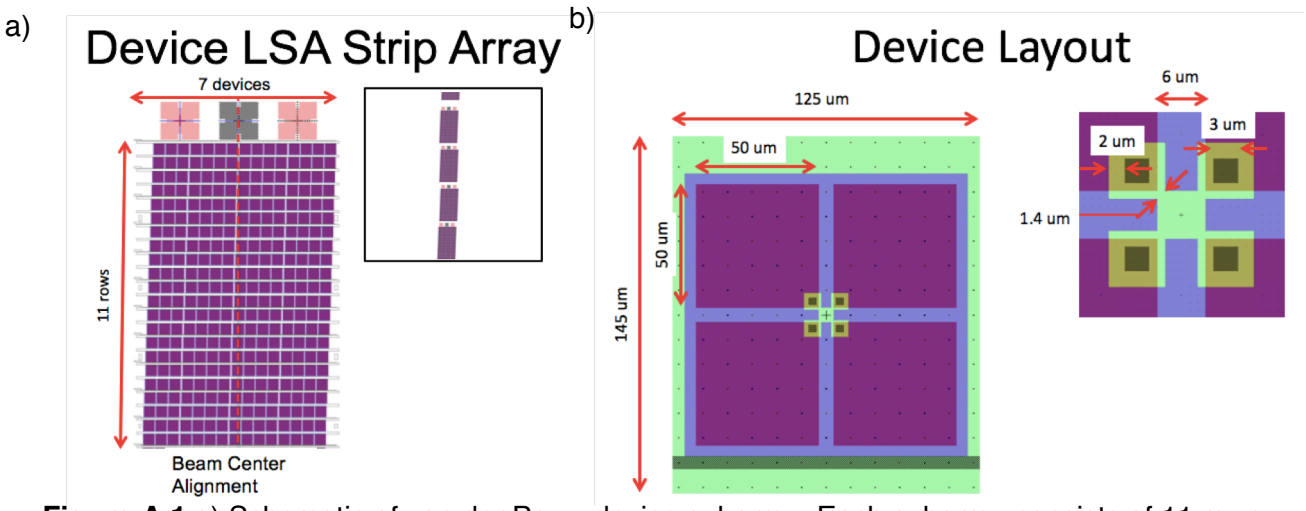

Figure A.1 a) Schematic of van der Pauw device subarray. Each subarray consists of 11 rows containing seven devices each. Above each subarray are alignment marks used to align the laser beam center during LSA. Inset is approximate scale of one device stripe on a 2 cm x 2 cm sample. (b) Schematic of the layout of each device. After the IGZO is deposited, blue areas indicate sections that were etched away while green areas represent the remaining active layer. Black areas indicate regions etched away to make the via channels while purple areas represent the metal contact pads deposited last.

Laser spike annealing was then used to rapidly anneal and crystallize the underlying IGZO films. With the laser aligned to the center of the device stripes on each sample, the lateral temperature profile created with this technique yields a peak annealing temperature gradient across the device rows, allowing for characterization as a function of peak annealing temperature.

LSA was used to initially irradiate samples with a CO_2 laser (10.6 μm wavelength, FWHM = 650 μm) with 45-55 W of laser power at dwell times of 300, 575, and 1000 μs. Following laser irradiation, 5 nm Cr and 80 nm Al contacts were deposited using a CHA thermal evaporator and photolithographically patterned over the devices.

However, substrates were lightly doped and did not absorb the CO_2 irradiation. It was determined that the fiber-coupled diode laser, at a 980 nm wavelength and a FWHM = 1.5 mm, would be more effective at annealing the samples. The metal contact pads were stripped with Transene Type A Al etchant in a 50 °C heated bath for 30 sec.

Samples were then annealed using the diode laser. To avoid lateral beam profile overlap, only every other device stripe, spaced approximately 6 mm apart, was annealed.

A.3.2 Four-point Probe Electrical Testing

Electrical measurements of the van der Pauw devices were conducted using a 4-point manual probe station with Signatone SE-20T Tungsten tips. A Keithley 2400 Source Measurement Unit (SMU) was used as a current source with a voltage compliance of 21 V. Contact resistance and 4-point van der Pauw resistance measurements were obtained.

A.3.3 Determination of Capacitive Behavior

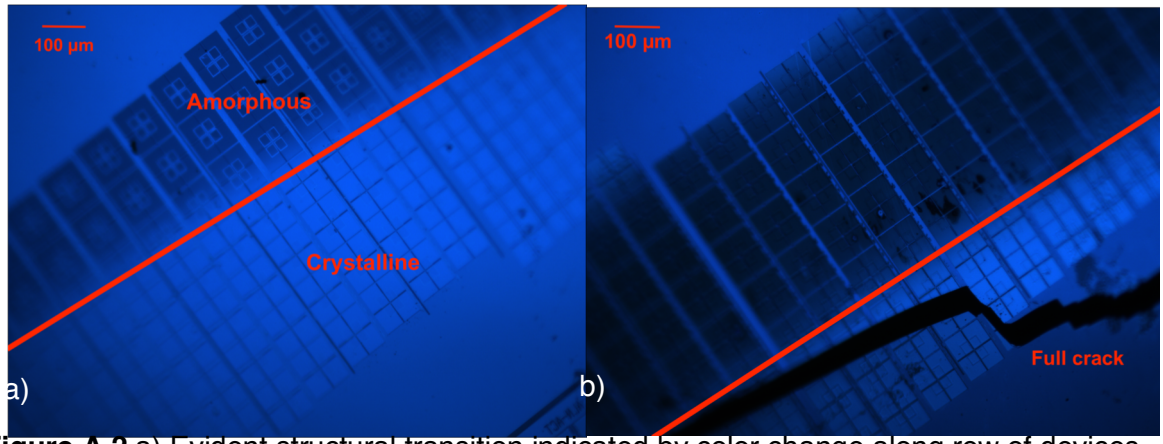

Figure A.2 a) Evident structural transition indicated by color change along row of devices on sample fabricated on low-doped Si substrate and annealed by diode laser at 10 ms dwell at 70.9 A. (b) Sample cracking in region of laser beam center under annealing conditions of 10 ms dwell and 97.2 A.

Figure A.2 shows photomicrographs of annealed stripes under the two 10 ms laser conditions at 70.9 and 97.2 A. Visual inspection confirms the structural transition from an amorphous structure to the crystalline phase within the lateral temperature gradient. The transition to a crystalline phase was expected to result in higher conductivity due to improved carrier mobility.

Initial resistance measurements ranged in the 60-200 MΩ range for contact and 4-point van der Pauw resistance, indicating essentially non-conducting films. Figure A.3 shows the current and voltage curves for a sweep in current from -10 nA to +10 nA with a compliance limit of 21 V.

The behavior observed in every resistance scan in Figure A.3 is consistent with the material acting as a capacitor. The parabolic IV curve shows the charging of the capacitor material with negative current up to a voltage of -12 V. When current is reversed, the material begins discharging symmetrically until the device is fully discharged. This evidence supported the hypothesis that a material in the van der Pauw device structure behaved as a capacitor under the application of current between 10 and 100 nA.

The capacitance of the van der Pauw dielectric device stack was calculated by measuring the time per scan and determining the time to charge to a known potential. A 51-point scan at 10 nA took 4.23 s or 82.9 ms per point. The total accumulated charge in the device was determined using $Q = \frac{1}{4} I_{scan} N_{pts} t_{pt}$, where I_{scan} is the scanning current, N_{pts} is the total number of points per scan, and t_{pt} is the time per point. The capacitance was determined as C=Q/V where 11 V is the maximum voltage magnitude observed at the point the current reverses from positive to negative. The total capacitance of the van der Pauw devices and measurement equipment was found to be approximately 0.96 nF.

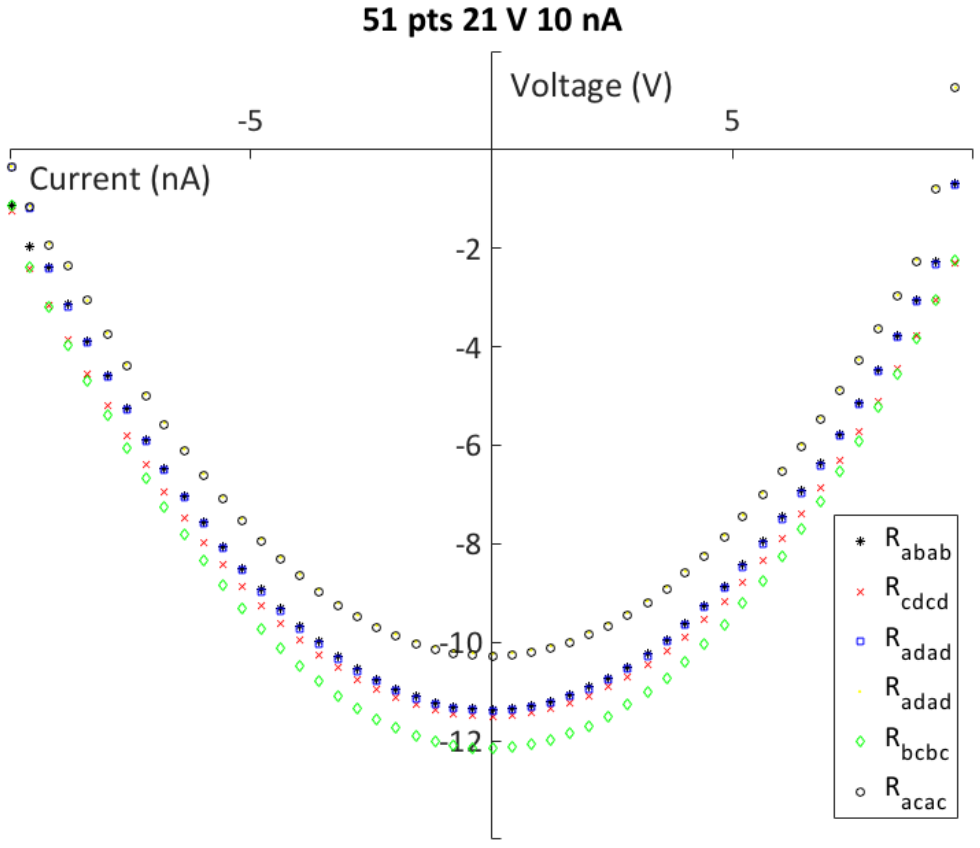

Figure A.3 4-point van der Pauw resistance measurements at 10 nA exhibited a parabolic IV curve, indicating the charging and discharging of current that is characteristic to capacitor behavior.

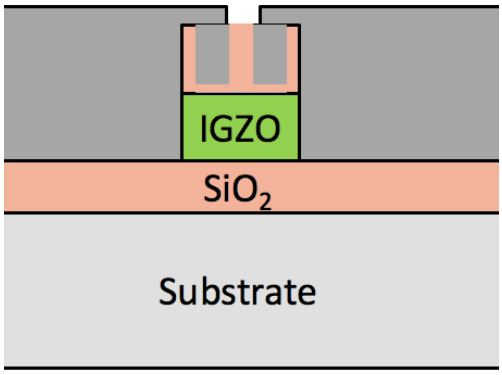

Figure A.4 Cross-section schematic of van der Pauw devices behaving as a capacitor. This schematic depicts the model where a thin layer of the passivating SiO_2 covering the active IGZO layer was not completely removed during the via etch. This would implicate the thin SiO_2 layer as the dielectric material responsible for the observed capacitor-like behavior.

The capacitance of the measurement equipment alone was determined by collecting a 51-point current scan at 10 nA with the measurement probe tips lifted off the sample; a capacitance of 1.06 nF was found. There is an inconsistency since the sample and measurement system capacitance should be larger than the system alone. This difference is thought to be an artifact of the parasitic effects occurring on the small 6 μm x 6 μm active material area. Taking the averages of the 4-point resistance scans, the magnitude of the difference between C_{total} and $C_{equipment}$ yields a device capacitance of 96 pF. The observed behavior was explained by determining which material in the van der Pauw device stack acted as a capacitor. During processing of the van der Pauw devices, the passivation layer was not completely etched resulting in a dielectric layer between the IGZO and the aluminum contacts, as modeled in the diagram in Figure A.4. The remnant SiO_2, which would be within the range of 1 nm to 30 nm, then formed the capacitor within a device cross-section shown in Figure A.4. In the thin film capacitor model, the capacitance was estimated using $C = \frac{\kappa \varepsilon_0 A}{t}$ where κ (3.9 for SiO_2) is the relative permittivity of the capacitor material, ε_0 is vacuum permittivity, A is the area of the capacitor, and t is the thickness of the layer [6]. The area of the unetched SiO_2 layer was considered as the area of the via channel contact areas, or 2.5 x 10^{-9} m^2. The thickness

required to achieve the measured capacitance value, called t_{req}, was determined to be 0.9 nm. This model is the most plausible explanation because the estimated range of thickness remaining after an under-etch is 1 to 30 nm and calculations show just under 1 nm SiO_2 in the via channels is needed to yield the device capacitance.

A.4 Furnace Annealing Conditions

While LSA is a primary annealing technique to crystallize amorphous IGZO films after deposition, furnace annealing is also used to control carrier concentration after deposition. Furnace annealing employs lower temperatures and longer timescales than LSA thus it cannot rapidly nucleate crystalline regions in thin films. However, this method can be used to adjust the carrier concentration in IGZO films by controlling the annealing gas. Annealing in an N_2 environment can result in loss of oxygen in the film and formation of more O_2 vacancies that would act as carriers. Similarly, samples can be annealed in an O_2 gas environment to promote the absorption of O_2 from atmosphere and a reduction of O_2 vacancies and carrier concentration. A quartz tube furnace was used to anneal IGZO subsamples in an N_2 gas environment for 20-60 minutes at 350-500 °C. A Cascade Microtech CPS-05 four-point resistance probe station was then used with a 100 mA scanning current to estimate the sheet resistance of the annealed films. It was found that annealing conditions of 40 minutes in 500 °C furnace with 7 sccm N_2 environment yielded a film with the lowest sheet resistance of 22 Ohm/□. This anneal shows that longer timescale annealing techniques can be used to achieve near-conductive films and future device fabrication recipes would benefit from a furnace annealing step designed to optimize conductivity.

A.4.1 Sheet resistance after LSA

It is known that LSA can affect IGZO thin film conductivity. LSA is normally performed in an ambient atmosphere, thus annealing can incorporate O_2 from the environment into the annealed

film, eliminating O_2 vacancies and reducing the carrier concentration. The most conductive subsample from the furnace annealing experiment was selected for LSA. Three sets of relative anneal conditions from the main X-ray experiment were chosen and replicated for this experiment: high peak anneal temperature, long dwell (1600 °C, 10 ms); low peak anneal temperature, long dwell (1500 °C, 10 ms); and low peak anneal temperature, short dwell (1500 °C, 250 us). The anneal stripe regions were then measured for sheet resistance using the four-point probe set up. The high peak anneal temperature, long dwell stripe yielded the lowest sheet resistance at 12.25 Ω/□, almost a fraction of two reduction over furnace annealing. This implies that the carrier loss from the anneal in O_2 was offset by another conductivity-enhancing change. It is likely that a crystalline transition occurred and improved the carrier mobility of the film enough to improve the overall carrier conductivity. In the cases of the other two anneal conditions, the middle stripe at low peak anneal temperature, long dwell (1500 °C, 10 ms) yielded a sheet resistance of 104.88 kΩ/□ and the end stripe at low peak anneal temperature, short dwell (1500 °C, 250 us) yielded even higher sheet resistance at 155.57 kΩ/□. As reflected in the measurements, it is clear O_2 absorption took place without a conductivity-enhancing change to reduce the carrier concentration so drastically without improving carrier mobility. The two stripes at low peak anneal temperatures yielded nonconductive films regardless of dwell time implying that changes in peak annealing temperature have a greater effect on the resulting film conductivity than changes in dwell.

BIBLIOGRAPHY

[1] T. Kamiya and H. Hosono, “Material characteristics and applications of transparent amorphous oxide semiconductors,” *NPG Asia Materials*, vol. 2, no. 1. pp. 15–22, 2010.

[2] D. M. Lynch, “Indium Gallium Zinc Oxide: Phase Formation and Crystallization Kinetics During Laser Spike Annealing,” Cornell University, 2017.

[3] K. Nomura, H. Ohta, A. Takagi, T. Kamiya, M. Hirano, and H. Hosono, “Room-temperature fabrication of transparent flexible thin-film transistors using amorphous oxide semiconductors,” *Nature*, vol. 432, no. 7016, pp. 488–492, 2004.

[4] S. Yamazaki, “New crystalline structure yields reliable thin-film transistors,” *SPIE Newsroom*, 2012.

[5] S. Wagner, H. Gleskova, I. C. Cheng, and M. Wu, “Silicon for thin-film transistors,” in *Thin Solid Films*, 2003, vol. 430, no. 1–2, pp. 15–19.

[6] V. O. Gupta, “A Survey on Stunning IGZO Technology.”

[7] K. Nomura, A. Takagi, T. Kamiya, H. Ohta, M. Hirano, and H. Hosono, “Amorphous Oxide Semiconductors for High-Performance Flexible Thin-Film Transistors,” *Jpn. J. Appl. Phys.*, 2006.

[8] J. K. Jeong, H. Won Yang, J. H. Jeong, Y.-G. Mo, and H. D. Kim, “Origin of threshold voltage instability in indium-gallium-zinc oxide thin film transistors,” *Appl. Phys. Lett.*, vol. 93, no. 12, p. 123508, Sep. 2008.

[9] K. H. Ji *et al.*, “Effect of high-pressure oxygen annealing on negative bias illumination stress-induced instability of InGaZnO thin film transistors,” *Appl. Phys. Lett.*, vol. 98, no. 10, p. 103509, Mar. 2011.

[10] H. S. Shin, B. du Ahn, Y. S. Rim, and H. J. Kim, “Annealing temperature dependence on the positive bias stability of IGZO thin-film transistors,” *J. Inf. Disp.*, vol. 12, no. 4, pp. 209–212, 2011.

[11] J. H. Kim *et al.*, “The effects of device geometry on the negative bias temperature instability of Hf-In-Zn-O thin film transistors under light illumination,” *Appl. Phys. Lett.*, vol. 98, no. 2, p. 023507, Jan. 2011.

[12] Y. J. Chung, U. K. Kim, E. S. Hwang, and C. S. Hwang, “Indium tin oxide/InGaZnO bilayer stacks for enhanced mobility and optical stability in amorphous oxide thin film transistors,” *Appl. Phys. Lett.*, vol. 105, no. 1, p. 013508, Jul. 2014.

[13] C. Y. Chung, B. Zhu, R. G. Greene, M. O. Thompson, and D. G. Ast, “High mobility, dual layer, c-axis aligned crystalline/amorphous IGZO thin film transistor,” *Appl. Phys. Lett.*, vol. 107, no. 18, p. 183503, Nov. 2015.

[14] J. Raja, K. Jang, H. H. Nguyen, T. T. Trinh, W. Choi, and J. Yi, “Enhancement of electrical stability of a-IGZO TFTs by improving the surface morphology and packing density of active channel,” *Curr. Appl. Phys.*, vol. 13, no. 1, pp. 246–251, Jan. 2013.

[15] K. Park *et al.*, “Reliability of Crystalline Indium-Gallium-Zinc-Oxide Thin-Film Transistors under Bias Stress with Light Illumination,” *IEEE Trans. Electron Devices*, vol. 62, no. 9, pp. 2900–2905, 2015.

[16] N. Kimizuka and T. Mohri, “Spinel, YbFe2O4, and $Yb_2Fe_3O_7$ types of structures for compounds in the In_2O_3 and $Sc_2O_3A_2O_3BO$ systems [A: Fe, Ga, or Al; B: Mg, Mn, Fe, Ni, Cu, or Zn] at temperatures over 1000°C,” *J. Solid State Chem.*, vol. 60, no. 3, pp. 382–384, Dec. 1985.

[17] N. Kimizuka, T. Mohri, Y. Matsui, and K. Siratori, “Homologous compounds, $InFeO_3(ZnO)_m$ (m = 1-9),” *J. Solid State Chem.*, vol. 74, no. 1, pp. 98–109, May 1988.

[18] N. Kimizuka, M. Isobe, and M. Nakamura, “Syntheses and single-crystal data of

homologous compounds, $In_2O_3(ZnO)_m$ (m = 3, 4, and 5), $InGaO_3(ZnO)_3$, and $Ga_2O_3(ZnO)_m$ (m = 7, 8, 9, and 16) in the In_2O_3–$ZnGa_2O_4$–ZnO System," *J. Solid State Chem.*, vol. 116, no. 1, pp. 170–178, Apr. 1995.

[19] N. Kimizuka and T. Mohri, "Structural classification of$RAO_3(MO)_n$ compounds (R =Sc, In, Y, or lanthanides; A =Fe(III), Ga, Cr, or Al; M =divalent cation; n = 1-11)," *J. Solid State Chem.*, vol. 78, no. 1, pp. 98–107, Jan. 1989.

[20] K. Nomura *et al.*, "Growth mechanism for single-crystalline thin film of $InGaO_3(ZnO)_5$ by reactive solid-phase epitaxy," *J. Appl. Phys.*, vol. 95, no. 10, pp. 5532–5539, May 2004.

[21] H.-G. Chen and Y.-S. Lin, "Epitaxial growth of superlattice $YbGaO_3(ZnO)_5$ and $InGaO_3(ZnO)_5$ films by the combination of sputtering and reactive solid phase epitaxy," *Thin Solid Films*, vol. 545, pp. 33–37, Oct. 2013.

[22] K. Nomura, T. Kamiya, H. Ohta, K. Ueda, M. Hirano, and H. Hosono, "Carrier transport in transparent oxide semiconductor with intrinsic structural randomness probed using single-crystalline $InGaO_3(ZnO)_5$ films," *Appl. Phys. Lett.*, vol. 85, no. 11, pp. 1993–1995, Sep. 2004.

[23] K. Nomura, H. Ohta, K. Ueda, T. Kamiya, M. Hirano, and H. Hosono, "Thin-film transistor fabricated in single-crystalline transparent oxide semiconductor.," *Science*, vol. 300, no. 5623, pp. 1269–72, May 2003.

[24] B. Du Ahn *et al.*, "Origin of Device Performance Degradation in InGaZnO Thin-Film Transistors after Crystallization," *Jpn. J. Appl. Phys.*, vol. 51, no. 1, p. 015601, Jan. 2012.

[25] G. H. Kim, H. S. Shin, B. Du Ahn, K. H. Kim, W. J. Park, and H. J. Kim, "Formation Mechanism of Solution-Processed Nanocrystalline InGaZnO Thin Film as Active Channel Layer in Thin-Film Transistor," *J. Electrochem. Soc.*, vol. 156, no. 1, p. H7, Jan. 2009.

[26] B. Zhu, D. M. Lynch, C. Chung, D. G. Ast, R. G. Greene, and M. O. Thompson, "Chemical Etch Rate and X-Ray Structure of Reactive Sputtered c-Axis Aligned Crystalline $In_xGa_yZn_zO_4$ Films," *ECS J. Solid State Sci. Technol.*, vol. 4, no. 5, pp. Q43–Q45, Apr. 2015.

[27] B. Zhu, D. M. Lynch, C. Chung, D. G. Ast, R. G. Greene, and M. O. Thompson, "45.2: Effects of RF Sputtering Parameters and Film Composition on C-Axis Aligned Crystalline (CAAC) IGZO Films," *SID Symp. Dig. Tech. Pap.*, vol. 46, no. 1, pp. 677–680, Jun. 2015.

[28] B. Zhu *et al.*, "Effects of RF Sputtering Parameters on C-axis Aligned Crystalline (CAAC) $InGaZnO_4$ Films Using Design of Experiment (DOE) Approach," *ECS J. Solid State Sci. Technol.*, vol. 5, no. 6, pp. P368–P375, Apr. 2016.

[29] S. Yamazaki, J. Koyama, Y. Yamamoto, and K. Okamoto, "15.1: Research, Development, and Application of Crystalline Oxide Semiconductor," *SID Symp. Dig. Tech. Pap.*, vol. 43, no. 1, pp. 183–186, 2012.

[30] M. Tsubuku *et al.*, "Negative-bias photodegradation mechanism in InGaZnO TFT," *Dig. Tech. Pap. - SID Int. Symp.*, vol. 44, no. 1, pp. 166–169, Jun. 2013.

[31] S. Yamazaki, "A possibility of crystalline Indium-Gallium-Zinc-Oxide," in *Proceedings of the 5th Asia Symposium on Quality Electronic Design, ASQED 2013*, 2013, pp. 1–5.

[32] S. Yamazaki *et al.*, "Properties of crystalline In-Ga-Zn-oxide semiconductor and its transistor characteristics," in *Japanese Journal of Applied Physics*, 2014, vol. 53, no. 4 SPEC. ISSUE.

[33] "To the Future... | IGZO:SHARP." [Online]. Available: http://www.sharp-world.com/igzo/. [Accessed: 30-Mar-2019].

[34] C.-Y. Chung, "High Mobility Of Sputtered $In_2Ga_2ZnO_7$ (IGZO) Thin Film Transistors (TFTs)," Cornell University, 2016.

[35] D. G. Ast, "(Invited) IGZO and a-Si:H : A Topological Constraint Theory View," *ECS*

Trans., 2017.
[36] K. E. Roach, “Millisecond crystallization kinetics of $InGaO_3(ZnO)_m$,” Cornell University, 2016.
[37] H.-W. Zan, W.-T. Chen, C.-W. Chou, C.-C. Tsai, C.-N. Huang, and H.-W. Hsueh, “Low Temperature Annealing with Solid-State Laser or UV Lamp Irradiation on Amorphous IGZO Thin-Film Transistors,” *Electrochem. Solid-State Lett.*, vol. 13, no. 5, p. H144, May 2010.
[38] P. Barquinha, L. Pereira, G. Gonçalves, R. Martins, and E. Fortunato, “The Effect of Deposition Conditions and Annealing on the Performance of High-Mobility GIZO TFTs,” *Electrochem. Solid-State Lett.*, vol. 11, no. 9, p. H248, Sep. 2008.
[39] H. Hosono, K. Nomura, Y. Ogo, T. Uruga, and T. Kamiya, “Factors controlling electron transport properties in transparent amorphous oxide semiconductors,” *J. Non. Cryst. Solids*, vol. 354, no. 19–25, pp. 2796–2800, May 2008.
[40] D. M. Lynch *et al.*, “Characterization of reactively sputtered c-axis aligned nanocrystalline $InGaZnO_4$,” *Appl. Phys. Lett.*, vol. 105, no. 26, p. 262103, Dec. 2014.
[41] R. T. Bell *et al.*, “Lateral Temperature-Gradient Method for High-Throughput Characterization of Material Processing by Millisecond Laser Annealing,” *ACS Comb. Sci.*, vol. 18, no. 9, pp. 548–558, 2016.
[42] C. Y. Chung, B. Zhu, D. G. Ast, R. G. Greene, and M. O. Thompson, “High mobility amorphous $InGaZnO_4$ thin film transistors formed by CO_2 laser spike annealing,” *Appl. Phys. Lett.*, vol. 106, no. 12, p. 123506, Mar. 2015.
[43] W. G. Hawkins and D. K. Biegelsen, “Origin of lamellae in radiatively melted silicon films,” *Appl. Phys. Lett.*, vol. 42, no. 4, pp. 358–360, Feb. 1983.
[44] K. Kato and A. Nukui, “Die Kristallstruktur des monoklinen Tief-Tridymits,” *Acta Crystallogr. Sect. B Struct. Crystallogr. Cryst. Chem.*, 2002.
[45] R. D. Shannon and C. T. Prewitt, “Synthesis and structure of phases in the In_2O_3:Ga_2O_3 system,” *J. Inorg. Nucl. Chem.*, vol. 30, no. 6, pp. 1389–1398, Jul. 1968.
[46] M. Nespolo, A. Sato, T. Osawa, and H. Ohashi, “Synthesis, Crystal Structure and Charge Distribution of $InGaZnO_4$. X-ray Diffraction Study of 20 kb Single Crystal and 50 kb Twin by Reticular Merohedry,” *Cryst. Res. Technol.*, vol. 35, no. 2, pp. 151–165, Feb. 2000.
[47] I. Keller, W. Assenmacher, G. Schnakenburg, and W. Mader, “Synthesis and Crystal Structures of $InGaO_3$ $(ZnO)_m$ ($m = 2$ and 3),” *Zeitschrift für Anorg. und Allg. Chemie*, vol. 635, no. 12, pp. 2065–2071, Oct. 2009.
[48] W. Schweika, *Disordered Alloys - Diffuse Scattering and Monte Carlo Simulations*. 1998.